Brymer *et al.*
Acta Neuropathologica Communications (2023) 11:27
https://doi.org/10.1186/s40478-023-01524-x

Acta Neuropathologica Communications

RESEARCH

Open Access

Asymmetric dysregulation of glutamate dynamics across the synaptic cleft in a mouse model of Alzheimer's disease

Kyle J. Brymer, Emily P. Hurley, Jessica C. Barron, Bandhan Mukherjee, Jocelyn R. Barnes, Firoozeh Nafar and Matthew P. Parsons*

Abstract

Most research on glutamate spillover focuses on the deleterious consequences of postsynaptic glutamate receptor overactivation. However, two decades ago, it was noted that the glial coverage of hippocampal synapses is asymmetric: astrocytic coverage of postsynaptic sites exceeds coverage of presynaptic sites by a factor of four. The fundamental relevance of this glial asymmetry remains poorly understood. Here, we used the glutamate biosensor iGluSnFR, and restricted its expression to either CA3 or CA1 neurons to visualize glutamate dynamics at pre- and postsynaptic microenvironments, respectively. We demonstrate that inhibition of the primarily astrocytic glutamate transporter-1 (GLT-1) slows glutamate clearance to a greater extent at presynaptic compared to postsynaptic membranes. GLT-1 expression was reduced early in a mouse model of AD, resulting in slower glutamate clearance rates at presynaptic but not postsynaptic membranes that opposed presynaptic short-term plasticity. Overall, our data demonstrate that the presynapse is particularly vulnerable to GLT-1 dysfunction and may have implications for presynaptic impairments in a variety of brain diseases.

Introduction

Tight control over the spatiotemporal dynamics of extracellular glutamate is necessary to prevent the toxic effects associated with extracellular glutamate accumulation [1]. High-affinity sodium-dependent excitatory amino acid transporters (EAATs) rapidly remove glutamate from the extracellular space, thereby promoting a high signal-to-noise ratio during synaptic neurotransmission and maintaining ambient glutamate concentrations at sub-toxic levels [2]. Glutamate transporter-1 (GLT-1) is the most abundant EAAT in the brain and is expressed in both astrocytes and presynaptic terminals [2, 3]. Impaired glutamate clearance, notably resulting from reduced GLT-1 expression and/or function, can trigger excitotoxic cell death that is often attributed to the overactivation of postsynaptic NMDA receptors [4–10]. As glutamate toxicity has been hypothesized to contribute to the pathogenesis of neurodegenerative diseases such as Alzheimer's disease (AD) [8, 11, 12], it is imperative that we increase our understanding of glutamate regulation in the healthy brain, and its dysregulation in disease.

Approximately 90–95% of the GLT-1 protein found in the brain is expressed in astrocytes [3, 13]. Two decades ago, it was first observed that the glial coverage of hippocampal synapses is asymmetric; that is, glial coverage of the postsynapse exceeds that of the presynapse by a factor of four [14]. A more recent study using 3D electron microscopy confirmed that the maximum astrocyte volume fraction around postsynaptic

*Correspondence:
Matthew P. Parsons
matthew.parsons@med.mun.ca
Division of Biomedical Sciences, Faculty of Medicine, Memorial University of Newfoundland, St. John's, NL A1B 3V6, Canada

© The Author(s) 2023. **Open Access** This article is licensed under a Creative Commons Attribution 4.0 International License, which permits use, sharing, adaptation, distribution and reproduction in any medium or format, as long as you give appropriate credit to the original author(s) and the source, provide a link to the Creative Commons licence, and indicate if changes were made. The images or other third party material in this article are included in the article's Creative Commons licence, unless indicated otherwise in a credit line to the material. If material is not included in the article's Creative Commons licence and your intended use is not permitted by statutory regulation or exceeds the permitted use, you will need to obtain permission directly from the copyright holder. To view a copy of this licence, visit http://creativecommons.org/licenses/by/4.0/. The Creative Commons Public Domain Dedication waiver (http://creativecommons.org/publicdomain/zero/1.0/) applies to the data made available in this article, unless otherwise stated in a credit line to the data.

densities was significantly larger than that surrounding presynaptic boutons [15]. The functional implications of this glial asymmetry—supported by modeling [14]—suggest that glutamate spillover in the hippocampus favors the overactivation of presynaptic autoreceptors, possibly as a negative feedback mechanism to attenuate release. It remains unknown whether glutamate clearance rates are differentially regulated across the synaptic cleft, and if so, how glutamate dynamics at pre- and postsynaptic microenvironments are impacted in diseases associated with GLT-1 impairment.

Impaired GLT-1 expression and/or function has been widely reported in AD animal models and in postmortem tissue [10, 16–23]. At present, we have a poor understanding of how GLT-1 dysfunction in AD alters the spatiotemporal dynamics of glutamate at pre- and postsynaptic membranes, and therefore a poor understanding of the glutamate receptor subtypes, and the side of the synapse on which they reside, that are most heavily impacted by GLT-1 impairment. Here, we used high-speed two-photon imaging following sparse injections of the glutamate biosensor iGluSnFR targeted to CA3 or CA1 to visualize real-time glutamate dynamics at pre- or postsynaptic microenvironments, respectively, in the stratum radiatum. Our data demonstrate that at CA3-CA1 hippocampal synapses in control mice, GLT-1 inhibition slows glutamate clearance to a greater extent at presynaptic compared to postsynaptic microenvironments. In the 3xTg mouse model of AD, GLT-1 dysfunction slowed glutamate clearance at presynaptic but not postsynaptic microenvironments, resulting in presynaptic mGluR overactivation that opposed short-term plasticity. As GLT-1 dysfunction is implicated in numerous brain diseases in addition to AD [24, 25], our experiments may also have broader implications for presynaptic vulnerability in a range of disease states.

Materials and methods

Animals

The experiments presented in Fig. 1 were conducted on acute brain slices obtained from male C57BL/6NCrl mice. Mice were ordered from Charles River at ~ 4 weeks of age and were acclimatized for at least 3 days upon arrival at Memorial University's animal care facility. All remaining experiments were conducted on acute brain slices obtained from male and female 3xTg mice (The Jackson Laboratory strain #034830) [26] and age-matched B6129SF2/J controls (The Jackson Laboratory strain #101045). No differences in male and female mice were noted for any of the measures obtained in the present study; therefore, the data were pooled from both sexes. All 3xTg and control mice were bred in our in-house colony at Memorial University. All mice were group housed in ventilated cage racks, provided with ad libitum access to standard chow and water, and maintained on a standard 12 h light/dark cycle. All experimental procedures were approved by Memorial University's Animal Care Committee and were conducted in accordance with the guidelines set by the Canadian Council on Animal Care.

Stereotaxic surgery

Surgical procedures were similar to previously published protocols from our lab [27, 28]. 3xTg mice, age-matched controls, and C57 mice were anesthetized by isoflurane inhalation (3%) and maintained with 1.5–2% isoflurane for the duration of the surgical procedure. Mice were secured within the ear bars of a standard stereotaxic apparatus (Stoetling), eye drops applied to lubricate the eyes, and a subcutaneous 0.9% saline injection containing 2 mg/kg meloxicam was provided to prevent dehydration during the procedure. When mice became unresponsive to a toe pinch a small amount of fur above the scalp was cut using scissors, and a 0.1 ml bolus of 0.2% lidocaine was injected below the scalp. A small incision was then made in the scalp surrounding bregma, and the underlying skull exposed. A hand drill was then used to carefully thin the skull at the desired coordinates from bregma, and a fine bent needle tip was used to peel back the last layer of skull to expose the underlying cortex while minimizing tissue damage. A Neuros 7002 Hamilton Syringe was attached to an infusion pump (Pump 11 Elite Nanomite; Harvard Apparatus), which was then secured to the stereotaxic frame. Animals used for calcium imaging received a total volume of 1 µl AAV1.Syn.Flex.GCaMP6f.WPRE.SV40 (a gift from Douglas Kim & Genie Project, Addgene plasmid # 100833) injected bilaterally into the hippocampus at an injection rate of 2 nl/s. The syringe was left in place for an additional 5 min after the injection to facilitate diffusion. The syringe was slowly withdrawn, incision sutured, and mice were given a subcutaneous injection of 0.5 ml of 0.9% saline before being placed on a heating pad for ~ 30 min to accelerate recovery. For glutamate imaging experiments, animals received a total of 1 µl of pAAV.hSyn.Flex.iGluSnFR.WPRE.SV40 (a gift from Loren Looger, Addgene plasmid # 98931) combined with a 1:50 or 1:100 dilution of 1 ul pAAV.hSyn.cre.WPRE.hGH. The following coordinates were used with respect to bregma: CA1: 2.6 mm posterior, 2.4 mm lateral, 1.1–1.3 mm ventral to brain surface [28]; CA3: 2 mm posterior, 2.3 mm lateral, 2.3 mm ventral [29]. The classification of pre- or postsynaptic iGluSnFR expression was determined on the day of imaging when viewing the transverse acute slice under the two-photon microscope. Slices were classified as "presynaptic" when CA3 but not

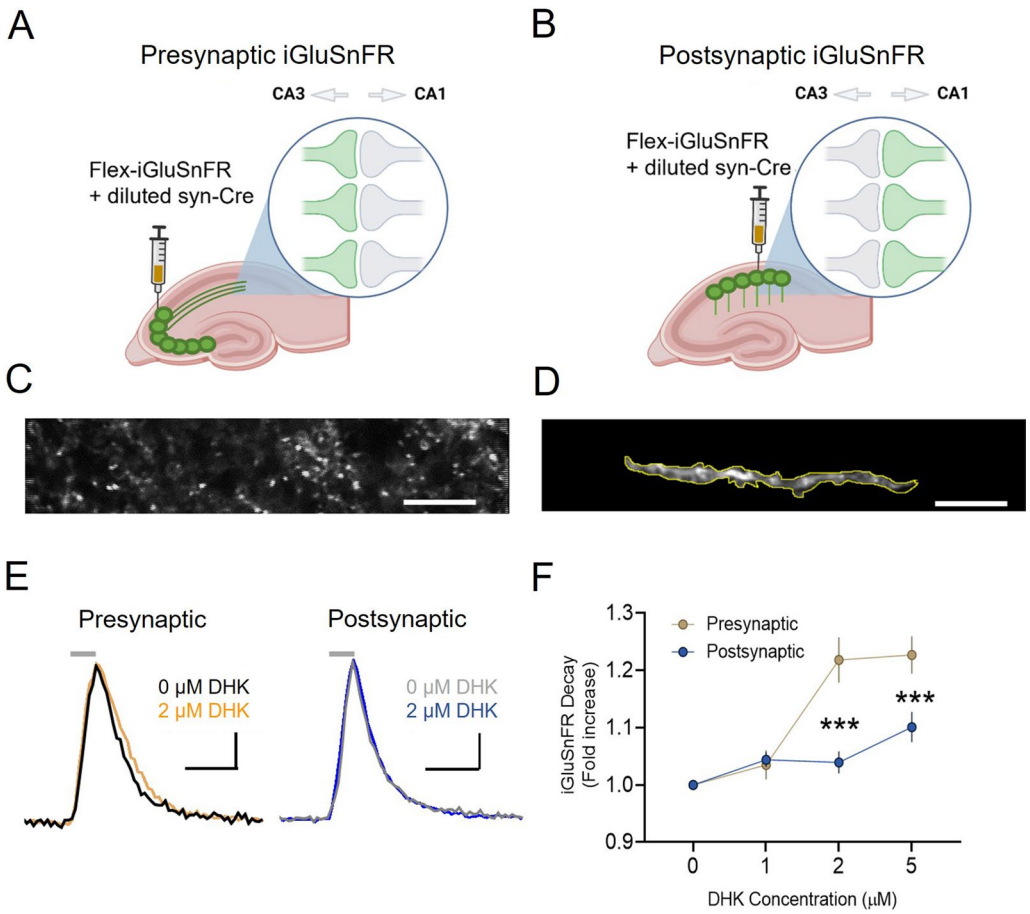

Fig. 1 Presynaptic microenvironments are more susceptible to partial GLT-1 inhibition than postsynaptic microenvironments. Schematic showing presynaptic (**A**) and postsynaptic **B** expression of iGluSnFR. Two-photon microscopy images with iGluSnFR expression obtained in CA1 showing presynaptic iGluSnFR expression with punctate expression pattern (**C**), or postsynaptic iGluSnFR expression of a single dendritic segment (**D**). **E** Evoked iGluSnFR responses (5 pulses, 100 Hz) in CA1 stratum radiatum with and without DHK application. Shown are traces for pre and postsynaptic microenvironments. **F** DHK application increases iGluSnFR decay tau to a greater extent at presynaptic compared to postsynaptic membranes. Horizontal lines above iGluSnFR traces indicate the timing and duration of electrical stimulation. Scale bars in C-D: 10 µm. Scale bars in E: 25%ΔF/F, 100 ms. DHK (2 µM) traces scaled to match the peak of DHK (0 µM traces). Error bars indicate s.e.m. *** $p < 0.001$

CA1 cell body iGluSnFR expression was present, with clear punctate iGluSnFR expression observed in CA1 stratum radiatum. Slices were classified as "postsynaptic" when CA1 cell body iGluSnFR expression was present, with clear apical dendrites observed in CA1 stratum radiatum running perpendicular to the CA1 cell body layer. For some experiments, iGluSnFR was expressed in astrocytes (using the above CA1 co-ordinates) by injecting 1 µl of pENN.AAV.GFAP.iGluSnFR.WPRE.SV40 (a gift from Loren Looger, plasmid # 98930).

Ceftriaxone treatment

6-month-old 3xTg and age-matched control mice were used for all ceftriaxone experiments. Similar to previous protocols from our lab [30, 31], mice were treated with ceftriaxone (200 mg/kg) or sterile saline via intraperitoneal injection for 5–7 days. 24 h after the last injection, mice were sacrificed and acute sections containing the hippocampus were obtained (described below).

Slice preparation

At 6 months of age (2–4 weeks after iGluSnFR injection), an age which corresponds to the emergence of an AD-like phenotype in 3xTg mice [26], mice were anesthetized with isoflurane and decapitated. A subset of experiments were performed on mice aged to 12 months, as indicated. For the experiments in Fig. 1, C57BL/6NCrl mice were sacrificed at 2 months of age. The brain was quickly removed and immersed in ice-cold oxygenated (95% O_2/5% CO_2) slicing solution consisting of (in mM)

125 NaCl, 2.5 KCI, 25 $NaHCO_3$, 1.25 NaH_2PO_4, 2.5 $MgCl_2$, 0.5 $CaCl_2$, and 10 glucose. Slices from the brains of the 12-month-old mice were prepared in N-methyl-D-glucamine (NMDG) and HEPES solutions to improve slice health as described previously [32]. Transverse hippocampal slices (350 µm) were obtained using a Precisionary compresstome. Slices were transferred to a holding chamber containing oxygenated ACSF for recovery 45 min before experimentation. The ACSF consisted of (in mM) 125 NaCl, 2.5 KCI, 25 $NaHCO_3$, 1.25 NaH_2PO_4, 1 $MgCl_2$, 2 $CaCl_2$, and 10 glucose. Slices for electrophysiology experiments were recovered at room temperature for a minimum of 90 min. Slices from the 12-month age group were transferred to NMDG ACSF after slicing with time-dependent sodium spiking applied exactly as described [32] and were then transferred to HEPES ACSF for an additional hour before use.

Imaging and image analysis

Glutamate imaging. After recovery, slices were transferred to the recording chamber of a Scientifica Hyperscope, and a peristaltic pump (MP-II; Harvard Apparatus) was used to perfuse oxygenated ACSF at a flow rate of 2 ml/min. As we used tissue from mice aged 6 and 12 months, most experiments were conducted at room temperature to help ensure maximal slice health for evoking clear iGluSnFR responses and recording clean and stable field excitatory postsynaptic potentials (fEPSPs). Some recordings were performed at a near-physiological temperature of 32 °C, as indicated in the results text. Glass stimulating electrodes were pulled using a Narishige PB-7 pipette puller to a resistance of 1–3 MΩ when filled with ACSF. Alexa Fluor 594 hydrazide sodium salt was added to the ACSF in the pipette to facilitate placement in the slice while two-photon imaging. iGluSnFR was excited using a Chameleon Vision II femtosecond pulsed laser tuned to 920 nm. iGluSnFR fluorescence was captured using a 16x/0.8NA objective (Nikon), and ScanImage 2019 was used to control all image acquisition parameters. The glass stimulating electrode was placed directly in the Schaffer collateral pathway within the stratum radiatum, at a depth of 50–100 µm below the slice surface, approximately 20–30 µm lateral (towards CA3) to the imaging region of interest (ROI). To visualize evoked iGluSnFR transients, fast resonant scanning was used with a 10 × zoom, and the imaging field was collapsed to 100 lines to achieve a frame rate of 153.6 frames per second. Clampex software (Molecular Devices) was used to send TTL triggers through the digital outputs of a Digidata 1550A (Molecular Devices) to trigger image acquisition and electrical stimulation (100 µs pulses, 75 µA) via an Iso-Flex stimulus isolator (AMPI). Five evoked iGluSnFR responses (20 s intervals) were averaged for each stimulation protocol. Values from the average file obtained from trials with presynaptic iGluSnFR expression were converted to Δ%*F*/*F*, and decay tau values were calculated in GraphPad Prism 9. Decay tau values were quantified starting at the offset of electrical stimulation (i.e. from the glutamate response at the end of the 5 or 100 pulse train to its return to baseline), similar to that described previously for widefield iGluSnFR [27, 28, 30, 31]. In slices with clear iGluSnFR expression in CA1 pyramidal neurons, single dendritic segments were identified running perpendicular to the CA1 cell body layer. To minimize the contribution from nearby axonal labeling to these postsynaptic signals, an ROI was drawn around the imaged dendritic segment and the "clear outside" function of ImageJ was used to restrict our quantified %ΔF/F values to the dendritic ROI.

Calcium imaging After recovery, slices were transferred to the recording chamber, and a peristaltic pump (MP-II; Harvard Apparatus) was used to perfuse oxygenated ACSF at a flow rate of 2 ml/min. Glass stimulating electrodes were pulled using a Narishige PB-7 pipette puller to a resistance of 1–3 MΩ when filled with ACSF. The stimulating electrode was placed directly in the Schaffer collateral pathway within the stratum radiatum, at a depth of 50–100 µm below the slice surface. Clampex software (Molecular Devices) was used to send TTL triggers through the digital outputs of a Digidata 1550A (Molecular Devices) for precise control over a LED illumination source (Prior, Lumen 300), an EM-CCD camera (Andor, iXon Ultra 897), and an Iso-flex stimulus isolator (AMPI). GCaMP6f responses to evoked neural activity were recorded with Andor Solis software, using 4 × 4 binning and an acquisition rate of 205 frames per second. Evoked GCaMP6f responses were quantified within a 10 × 10 pixel ROI (1 pixel at 4 × 4 binning = 16 µm) placed adjacent to the location of the stimulating electrode and converted to %Δ*F/F*. The area under the curve (AUC) was calculated before and after bath application of D-APV (50 µM) to determine how much of the pre- or postsynaptic calcium response was NMDA receptor-dependent.

Electrophysiology

Acute hippocampal slices from 6-month-old 3xTg and age-matched control mice were placed in the recording chamber and were left for a minimum of 10 min before electrode placement. Room temperature ACSF was superfused into the recording chamber at a rate of 2 ml/min. A glass stimulating electrode filled with ACSF (1–3 MΩ) was placed in the stratum radiatum to stimulate Schaffer collateral fibres in the CA1 region. A glass

recording electrode filled with ACSF (1–3 MΩ) was next placed ~ 400 µm from the stimulating electrode, and signals were amplified and low-pass filtered at 10 kHz with a Multiclamp 700B amplifier (Molecular Devices). Using an inter-pulse interval of 50 ms, we measured paired-pulse ratios (PPR) by dividing the fEPSP amplitude evoked by the second stimulus by the that induced by the first. We first recorded PPR for 3 min to establish a baseline, then applied HFS (3 × 100 Hz, 1 s, 10 s inter-train intervals). After HFS, PPR was again recorded for 5 min. All data were collected and analyzed using pClamp 10 software (Molecular Devices).

Pharmacology

All drugs used in the current experiments were from Tocris Bioscience. Drugs used in the study and their concentrations are as follows: dihydrokainic acid (DHK), a competitive and selective GLT-1 blocker (300 µM; low DHK experiments used 1, 2, or 5 µM as indicated); $_{DL}$-threo-β-benzloxsapartic acid ($_{DL}$-TBOA), a competitive and nonselective EAAT blocker (100 µM); DNQX disodium salt, an AMPA/kainate receptor antagonist (20 µM); D-APV, a selective NMDA receptor antagonist (50 µM); MSOP, a selective group III metabotropic glutamate receptor antagonist (100 µM); and MTEP hydrochloride, a selective mGluR5 antagonist (100 µM). In DHK, TBOA, or MSOP/MTEP experiments, slices were incubated for 5–10 min before imaging or electrophysiology was conducted.

GLT-1 immunohistochemistry

Mice were perfused and brains were cryoprotected in 30% sucrose until sunk. Whole brains were rapidly frozen and sliced at 20 µm on a cryostat (Leica CM3050 S), and sections were mounted directly onto gelatin-coated glass slides and stored at − 80 ℃ until use. Day 1: Slides were removed from -80℃ and brought to room temperature, and a Dako pen was used to trace the perimeter of the slide. Slides were washed three times in 0.01 M PBS for 10 min each. Slides were then incubated in blocking serum (0.01 M PSB with 5% BSA + 0.2% Triton-X) for one hour. After blocking, slides were incubated in primary antibody (guinea pig anti-GLT-1, 1:500, Abcam, AB1783) overnight at 4 ℃. The specificity of this particular antibody is nicely demonstrated in a recent study using Western blot and immunohistochemistry showing clear GLT-1 reductions in GLT-1$^{\pm}$ mice and significant GLT-1 upregulation following ceftriaxone treatment [33]. Slides were then washed three times in 0.01 M PBS for 10 min each and incubated in secondary antibody (Alexa fluor 647-conjugated donkey anti-guinea pig, 1:500, Jackson Immunoresearch Labs) at room temperature for 2 h. After the final washes in 3 times in 0.01 M PBS for 10 min each, slides were cover slipped using Dako mounting medium containing DAPI. Images of CA1 stratum radiatum were obtained at 20 × on a Zeiss AxioObserver. GLT-1 intensity was calculated within an ROI in the stratum radiatum using ImageJ. For GLT-1 immunohistochemistry and imaging, all samples were processed at the same time and imaging parameters, including LED intensity and exposure times, were kept constant.

Experimental design and statistics

Statistical tests used included unpaired t-tests and two-way repeated-measures (RM) ANOVA with Bonferroni post-hoc tests. The statistical test used for each experiment is indicated in the results text. *P* values of < 0.05 were considered significant. In iGluSnFR experiments, the same slice received both 5 pulses and 100 pulses of electrical stimulation, therefore resulting in a repeated-measures two-way ANOVA design. For these datasets, we report the overall genotype p-value (WT compared to 3xTg), the overall pulse number p-value (5 pulses compared to 100 pulses) and any interaction effects between the two factors, as indicated. For any significant genotype or interaction effects, Bonferroni post-hoc tests were used to compare genotypes at 5 pulses as well as at 100 pulses. Where indicated, *N* and *n* refer to the number of animals and slices used in each experiment, respectively. For postsynaptic analyses, only a single dendritic segment was analyzed in a given slice. In many cases, more than one slice experiment was obtained from a given animal, and statistically, we treat the slice value n as independent datapoints, rather than averaging all slice responses from a given animal. Importantly, nested Chi-square values of individual datasets were all non-significant ($P > 0.05$), demonstrating that there were no significant differences between subcolumns (i.e. from one animal to the next in a given genotype). Thus, significant results presented in the present study are unlikely to arise as a result of pseudoreplication [34].

Results

The presynapse is more sensitive than the postsynapse to GLT-1 inhibition

The previously observed asymmetric glial coverage across the synapse [14, 15] suggests that presynaptic membranes may be more susceptible to glutamate spillover than postsynaptic membranes. To test for functional evidence of a presynaptic vulnerability to glutamate spillover during partial GLT-1 impairment, we examined the effects of sub-saturating concentrations (1–5 µM, saturating = 300 µM [27]) of the GLT-1 inhibitor DHK on real-time glutamate dynamics sensed at presynaptic (Fig. 1A, C) or

postsynaptic (Fig. 1B, D) membranes using sparse injections of iGluSnFR targeted to CA3 or CA1, respectively. These experiments were performed on healthy control (C57) mice. Both D-APV (50 μM) and DNQX (20 μM) were added to the bath solution, and two-photon microscopy was used to capture synaptically-evoked iGluSnFR transients in acute hippocampal slices. Clear iGluSnFR transients (Fig. 1E) were evoked by 5 pulses of electrical stimulation (100 Hz; 75 μA) applied to the Schaffer collaterals, and we monitored the glutamate response in baseline conditions and then to increasing sub-saturating concentrations of DHK. The decay tau of evoked iGluSnFR transients were used to quantify relative changes in the rate of glutamate clearance as described previously [24, 27, 28, 30, 31, 35]. iGluSnFR decay was more sensitive to partial GLT-1 inhibition when iGluSnFR was expressed presynaptically compared to postsynaptically (Fig. 1F; presynaptic N = 3, n = 5; postsynaptic N = 3, n = 8; RM two-way ANOVA: $p_{DHK} < 0.001$; $p_{location} = 0.004$; $p_{interaction} < 0.001$). Specifically, 2 μM and 5 μM DHK significantly slowed presynaptic iGluSnFR decay to a greater extent than postsynaptic iGluSnFR (Bonferroni $p < 0.001$ for both 2 μM and 5 μM). Raw decay tau values were not significantly different prior to DHK application, although the average decay tau was a bit higher for postsynaptic responses (presynaptic: 64.9 ± 7.4 ms; postsynaptic: 82.9 ± 11.2 ms; t-test $p = 0.182$). Thus, at CA3-CA1 synapses in control mice, presynaptic membranes appear to be more sensitive to the effects of partial GLT-1 inhibition, in agreement with the morphological asymmetry of glial membranes favoring postsynaptic protection at the expense of the presynapse [14, 15]. Our methodological approach to visualize glutamate transients at pre- or postsynaptic membranes is similar to one described recently in detail [36]. As a positive control to help confirm our ability to separate pre- and postsynaptic biosensor responses with our AAV injections, we injected WT mice (2–4 months) with the calcium indicator GCaMP6f into either CA3 (presynaptic expression) or CA1 (postsynaptic expression). Calcium responses in the stratum radiatum were induced by high frequency stimulation (HFS; 100 pulses, 100 Hz) applied to the Schaffer collaterals; this stimulation protocol is commonly used to evoke long-term potentiation (LTP) that is dependent upon calcium influx through postsynaptic NMDA receptors (NMDARs) [37, 38]. We reasoned that NMDAR blockade with D-APV should significantly block the postsynaptic calcium response to HFS, while having minimal or no effect on presynaptic calcium responses. Indeed, postsynaptic GCaMP6f responses to HFS were significantly inhibited by NMDAR antagonism, while presynaptic GCaMP6f responses were completely unaffected by D-APV (Additional file 1: Fig. 1A-C; presynaptic n = 6, postsynaptic n = 11; t-test: $p < 0.001$). These data demonstrate that our AAV injections can effectively isolate pre- and postsynaptic membrane responses to evoked activity.

Impaired glutamate clearance at presynaptic microenvironments in 3xTg mice

Our low concentration DHK experiments above suggest partial GLT-1 inhibition slows glutamate clearance to a greater extent at presynaptic compared to postsynaptic microenvironments. GLT-1 function and/or expression is partially decreased in a variety of neurodegenerative diseases, including AD [24]. Therefore, we hypothesized that a similar presynaptic vulnerability to glutamate uptake deficits may be apparent in 3xTg mice, a commonly-used mouse model of AD that presents with age-dependent amyloid and tau pathology [26]. Acute slices were obtained from mice at six months of age, and neural activity was evoked with a short burst (5 pulses at 100 Hz) as well as with a longer train (100 pulses at 100 Hz) of electrical stimulation, the latter being known to overwhelm the glutamate uptake system [27, 39]. Despite significantly reduced GLT-1 expression in 3xTg mice at this age (Additional file 1: Fig. 2; WT n = 12, 3xTg n = 10; t-test: $p = 0.002$), postsynaptic iGluSnFR decay did not differ between the genotypes, even when challenged with the longer train of neural activity (Fig. 2A-E; WT N = 7, n = 14; 3xTg N = 6, n = 14; RM two-way ANOVA: $p_{pulsenumber} < 0.001$; $p_{genotype} = 0.285$; $p_{interaction} = 0.602$). Postsynaptic iGluSnFR response peaks also did not differ between the two genotypes (Additional file 1: Fig. 3A; $p_{pulsenumber} < 0.001$; $p_{genotype} = 0.418$; $p_{interaction} = 0.418$).

In contrast, presynaptic iGluSnFR decay was significantly slower in 3xTg compared to WT mice, specifically when challenged with the longer train of activity (Fig. 2F-J; WT N = 6, n = 12; 3xTg N = 6, n = 11; RM two-way ANOVA: $p_{pulsenumber} < 0.001$; $p_{genotype} = 0.021$; $p_{interaction} = 0.031$). At 5 pulses of stimulation, 3xTg and WT mice did not differ in time taken to clear extracellular glutamate (Bonferroni $p = 0.999$) but increasing the number of pulses to 100 revealed a clear deficit in glutamate clearance in 3xTg mice (Bonferroni $p = 0.003$), demonstrating that the deficit is only revealed when the glutamate transporter system is challenged with a long duration of activity. The maximum amount of glutamate released was not different between the two genotypes, as the peak responses of presynaptic iGluSnFR expression was similar between WT and 3xTg mice (Additional file 1: Fig. 3B; RM

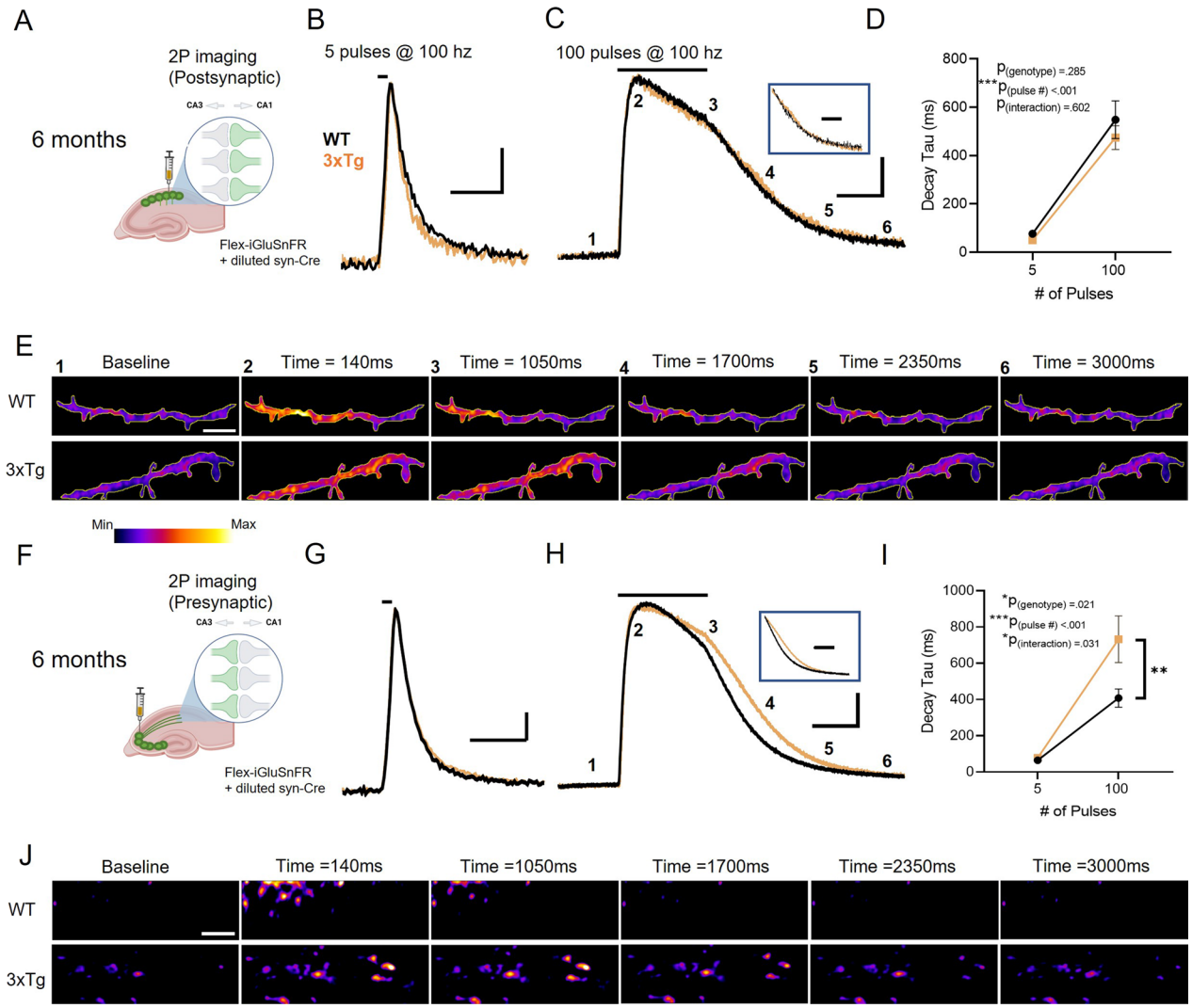

Fig. 2 Slow glutamate clearance at pre- but not postsynaptic microenvironments in the 6-month-old 3xTg hippocampus. **A**–**D** Postsynaptic iGluSnFR expression in CA1 dendrites. **A** Average postsynaptic iGluSnFR responses to 5 pulses (B) and 100 pulses **C** of electrical stimulation (100 Hz) in six-month-old WT (black) and 3xTg (orange) mice. Grouped data shown in D. **E** Representative images depicting the postsynaptic iGluSnFR response in 6-month-old WT (top row) and 3xTg (bottom row) mice evoked by 100 pulses of electrical stimulation (100 Hz). **F**–**I** Presynaptic iGluSnFR expression in CA1 dendrites (**F**). Average iGluSnFR responses to 5 pulses (**G**) and 100 pulses **H** of electrical stimulation (100 Hz) in six-month-old WT (black) and 3xTg (orange) mice. Grouped data shown in I. **J** Representative images depicting the presynaptic iGluSnFR response in 6-month-old WT (top row) and 3xTg (bottom row) mice evoked by 100 pulses of electrical stimulation (100 Hz). Boxed traces in C and H depict average iGluSnFR traces normalized to the iGluSnFR value at the end of the one-second stimulation. Black lines above iGluSnFR traces indicate the timing and duration of electrical stimulation. Scale bars in B, G: 5%ΔF/F, 200 ms. Scale bars in C, H: 20% ΔF/F, 500 ms. 3xTg traces scaled to match the peak of WT traces. Scale bar in E: 10 µm. Error bars indicate s.e.m. ** $p < 0.01$, *** $p < 0.001$

two-way ANOVA: $p_{pulsenumber} < 0.001$; $p_{genotype} = 0.289$; $p_{interaction} = 0.949$). For the 100 pulse data, responses were strong enough to obtain a clear iGluSnFR signal when the ROI was reduced to cover a putative single synapse. Using the same analysis approach, but restricting the measurements to individual responsive iGluSnFR puncta representative of putative single synapses, we found significantly increased decay tau values in 3xTg mice compared to WT (Additional file 1: Fig. 4A-C, $p < 0.0001$) and a higher fraction of putative synapses with slower decay values (Additional file 1: Fig. 4D; Kolmogorov–Smirnov test $p = 0.0003$). Furthermore, the 3xTg dataset was more variable than the WT dataset ($F_{31,34} = 10.79$, $p < 0.0001$), suggesting that the overall deficit we observe at presynaptic microenvironments may be driven by a subset of synapses rather than a global effect at all terminals.

The observed impairment of glutamate clearance at presynaptic but not postsynaptic membranes in 3xTg mice was also observed in a separate cohort of mice where the ACSF was heated to 32 ℃ (Additional file 1: Fig. 5; Postsynaptic: WT N = 3, n = 9; 3xTg N = 3, n = 9; RM two-way ANOVA: $p_{pulsenumber} < 0.001$; $p_{genotype} = 0.500$; $p_{interaction} = 0.353$; Presynaptic: WT N = 3, n = 8; 3xTg N = 4, n = 10; RM two-way ANOVA: $p_{pulsenumber} < 0.001$; $p_{genotype} = 0.030$; $p_{interaction} = 0.026$).

The above experiments were conducted in 6-month-old mice. In the 3xTg AD model, this age corresponds to the early emergence of an AD-like phenotype, including mild spatial- memory impairment and deficits in synaptic transmission [26, 40]. Next, we asked if our observed asymmetric dysregulation of glutamate clearance across the synaptic cleft persisted to a later disease stage, or whether more global impairments (i.e. at both pre- and postsynaptic microenvironments) could be observed. At

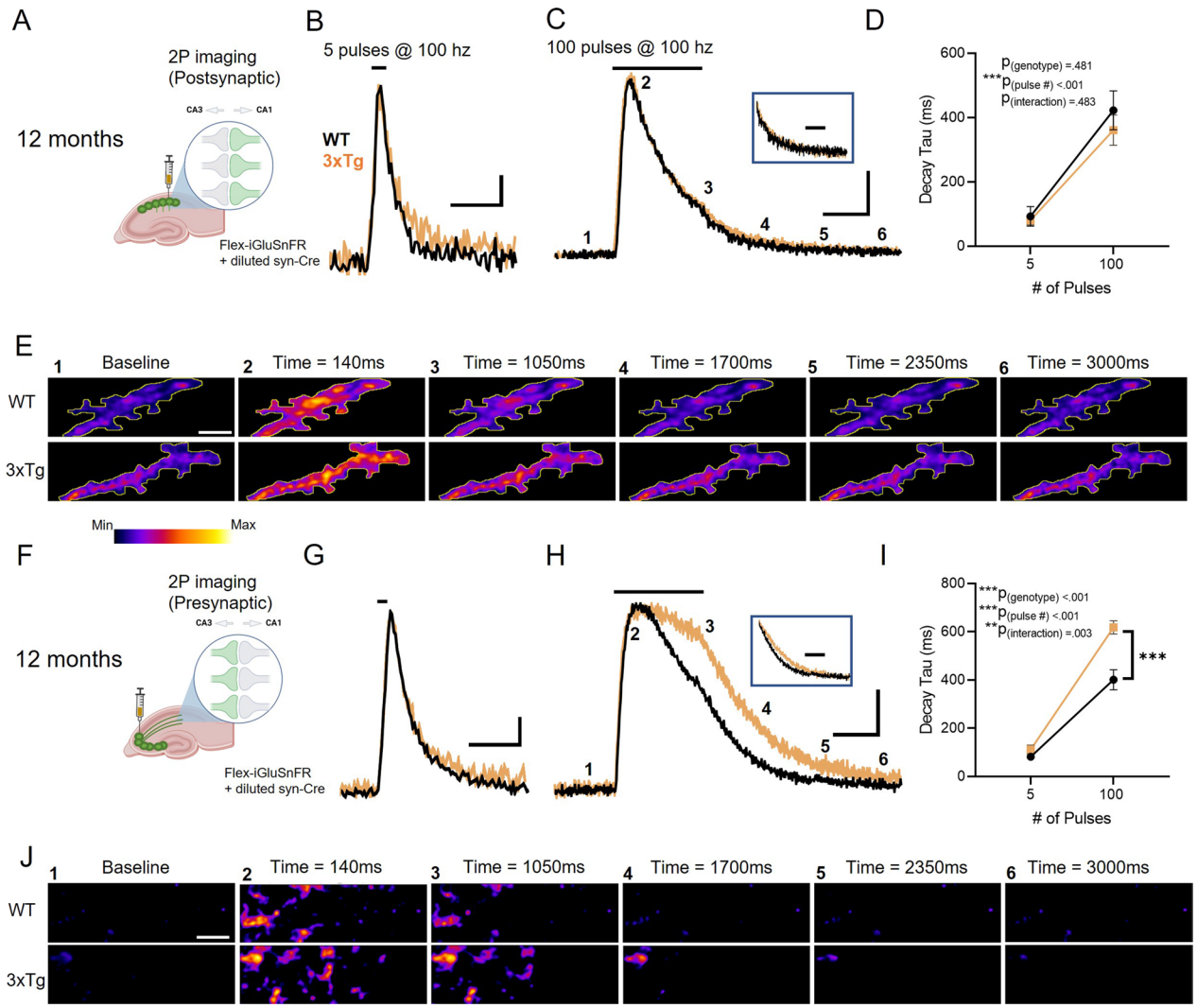

Fig. 3 Slow glutamate clearance at pre- but not postsynaptic microenvironments in the 12-month-old 3xTg hippocampus. **A**–**D** Postsynaptic iGluSnFR expression in CA1 dendrites (A). Average postsynaptic iGluSnFR responses to 5 pulses (**B**) and 100 pulses **C** of electrical stimulation (100 Hz) in twelve-month-old WT (black) and 3xTg (orange) mice. Grouped data shown in D. **E** Representative images depicting the postsynaptic iGluSnFR response in twelve-month-old WT (top row) and 3xTg (bottom row) mice evoked by 100 pulses of electrical stimulation (100 Hz). F–**I** Presynaptic iGluSnFR expression in CA1 dendrites (**F**). Average iGluSnFR responses to 5 pulses (**G**) and 100 pulses **H** of electrical stimulation (100 Hz) in twelve-month-old WT (black) and 3xTg (orange) mice. Grouped data shown in I. **J** Representative images depicting the presynaptic iGluSnFR response in twelve-month-old WT (top row) and 3xTg (bottom row) mice evoked by 100 pulses of electrical stimulation (100 Hz). Boxed traces in C and H depict average iGluSnFR traces normalized to the iGluSnFR value at the end of the one-second stimulation. Black lines above iGluSnFR traces indicate the timing and duration of electrical stimulation. Scale bars in B, G: 5%ΔF/F, 200 ms. Scale bars in C, H: 20%ΔF/F, 500 ms. 3xTg traces scaled to match the peak of WT traces. Scale bar in E: 10 µm. Error bars indicate s.e.m. ** $p < 0.01$, *** $p < 0.001$

12 months of age, 3xTg mice continued to display similar iGluSnFR responses as control mice when iGluSnFR was expressed in CA1 dendrites (Fig. 3A-E; WT N = 5, n = 10; 3xTg N = 5, n = 12; RM two-way ANOVA: $p_{pulsenumber} < 0.001$, $p_{genotype} = 0.481$, $p_{interaction} = 0.483$). Similar to our findings at six months, when expressed presynaptically, iGluSnFR decay tau values were significantly longer in 3xTg mice compared to WT (Fig. 3F-J; WT N = 4, n = 8; 3xTg N = 4, n = 12; RM two-way ANOVA: $p_{pulsenumber} < 0.001$, $p_{genotype} < 0.001$, $p_{interaction} = 0.003$). Again, glutamate clearance was significantly slower in 3xTg mice following 100 pulses (Bonferroni $p < 0.001$) but not 5 pulses (Bonferroni $p = 0.380$), suggesting that glutamate transporters need to be overwhelmed [27, 39] to observe a clear genotype difference. Together, these data demonstrate relative postsynaptic protection and presynaptic vulnerability to glutamate uptake impairments in both early and later disease stages in 3xTg mice. All remaining experiments were conduced on mice six months of age.

GLT-1 dysfunction underlies the slow glutamate clearance at 3xTg presynaptic microenvironments

Glutamate uptake in the hippocampus is mediated by GLT-1, GLAST and, to a lesser extent, EAAC1 [1, 24]. To determine whether the slow glutamate clearance observed at presynaptic membranes in 3xTg mice was due specifically to GLT-1 dysfunction, we probed the contribution of GLT-1 to overall glutamate clearance rates by bath applying a saturating concentration of DHK (300 µM [27]), applied in the presence of 50 µM D-APV and 20 µM DNQX. We then quantified the GLT-1 decay ratio, calculated by the decay tau fold increase induced by DHK; a larger decay ratio being indicative of a larger contribution of GLT-1 in the overall glutamate clearance rate [27, 41]. When we applied DHK to slices with presynaptic iGluSnFR expression, we found that the GLT-1 decay ratio was significantly reduced in 3xTg mice (Fig. 4A-C; WT N = 5, n = 10; 3xTg N = 3, n = 11; RM two-way ANOVA: $p_{pulsenumber} < 0.001$; $p_{genotype} = 0.004$; $p_{interaction} = 0.093$). Peak iGluSnFR responses were not significantly different in the two genotypes following DHK application (Additional file 1: Fig. 6A; RM two-way ANOVA: $p_{pulsenumber} < 0.001$; $p_{genotype} = 0.320$; $p_{interaction} = 0.029$). Next, we asked whether GLT-1 upregulation via ceftriaxone could reverse the glutamate clearance deficit seen in 3xTg mice. We, like many others, have shown that 5–7 consecutive days of ceftriaxone (200 mg/kg, i.p.) administration increases GLT-1 in the hippocampus [30]. Saline-treated mice showed the same effect as we had observed previously; namely, that glutamate clearance at presynaptic microenvironments is significantly slower in 3xTg mice. However, in these slices with presynaptic iGluSnFR expression, ceftriaxone completely restored 3xTg glutamate clearance rates to WT levels (Fig. 4D-F WT saline N = 3, n = 8; 3xTg saline N = 5, n = 11; WT ceftriaxone N = 3, n = 9; 3xTg ceftriaxone N = 3, n = 10; RM two-way ANOVA: $p_{pulsenumber} < 0.001$; $p_{genotype} < 0.001$; $p_{interaction} = 0.008$). Together, these results demonstrate that the prolonged glutamate actions at presynaptic membranes in the stratum radiatum is due to GLT-1 impairment in 3xTg mice.

Next, we repeated the same DHK and ceftriaxone experiments, but for postsynaptic iGluSnFR responses isolated in individual CA1 dendrites. In stark contrast to presynaptic iGluSnFR, we found that that the postsynaptic GLT-1 decay ratio was enhanced, rather than reduced, in 3xTg mice (Fig. 5A-C; WT N = 3, n = 9; 3xTg N = 4, n = 11; RM two-way ANOVA: $p_{pulsenumber} < 0.001$; $p_{genotype} = 0.011$; $p_{interaction} = 0.015$). Peak glutamate levels remained unchanged between the genotypes in the presence of DHK (Additional file 1: Fig. 6B; RM two-way ANOVA: $p_{pulsenumber} < 0.001$; $p_{genotype} = 0.087$; $p_{interaction} = 0.379$). Again, in contrast to presynaptic iGluSnFR expression, ceftriaxone had no significant effect on postsynaptic iGluSnFR dynamics (Fig. 5D-F; WT saline $N = 5$, $n = 8$; 3xTg saline $N = 5$, $n = 8$; WT ceftriaxone $N = 3$, $n = 10$; 3xTg ceftriaxone $N = 3$, $n = 8$; RM two-way ANOVA: $p_{pulsenumber} < 0.001$; $p_{genotype} = 0.157$; $p_{interaction} = 0.175$). While this postsynaptic dataset did not reach statistical

(See figure on next page.)

Fig. 4 GLT-1 is dysfunctional in presynaptic microenvironments of the 3xTg hippocampus. **A** Average presynaptic iGluSnFR response to 5 (left) and 100 pulses (right) of electrical stimulation (100 Hz) in WT (top; black and grey) and 3xTg mice (bottom; orange and grey) before and after DHK application. Grey traces denote average iGluSnFR response before DHK application. **B** GLT-1 decay ratio in WT and 3xTg mice, calculated by the fold increase in iGluSnFR decay induced by a saturating concentration of the GLT-1 inhibitor DHK. **C** Representative images depicting the presynaptic iGluSnFR response in the presence of DHK in WT (top row) and 3xTg (bottom row) mice evoked by 100 pulses of electrical stimulation (100 Hz). **D** Average presynaptic iGluSnFR responses to 5 (left) and 100 pulses (right) of stimulation in WT-saline (black), 3xTg-saline (orange), WT-ceftriaxone (Cef; blue), and 3xTg-ceftriaxone-treated mice (pink). **E** iGluSnFR decay tau in saline- or ceftriaxone-treated WT and 3xTg mice. **F** Representative images depicting the presynaptic iGluSnFR response in WT-saline (top row), 3xTg-saline (second row), WT-ceftriaxone (third row), and 3xTg-ceftriaxone-treated mice (bottom row) evoked by 100 pulses of electrical stimulation (100 Hz). Black lines above iGluSnFR traces indicate the timing and duration of electrical stimulation. Scale bars in A: 10%ΔF/F, 500 ms (left) and 30%ΔF/F, 1000 ms (right). DHK traces scaled to match the peak of control (without DHK) traces. Scale bars in D: 10%ΔF/F, 200 ms (left) and 30%ΔF/F, 500 ms (right). 3xTg traces scaled to match the peak of WT traces. Scale bar in E: 10 µm. Error bars indicate s.e.m. ** $p < 0.01$, *** $p < 0.001$

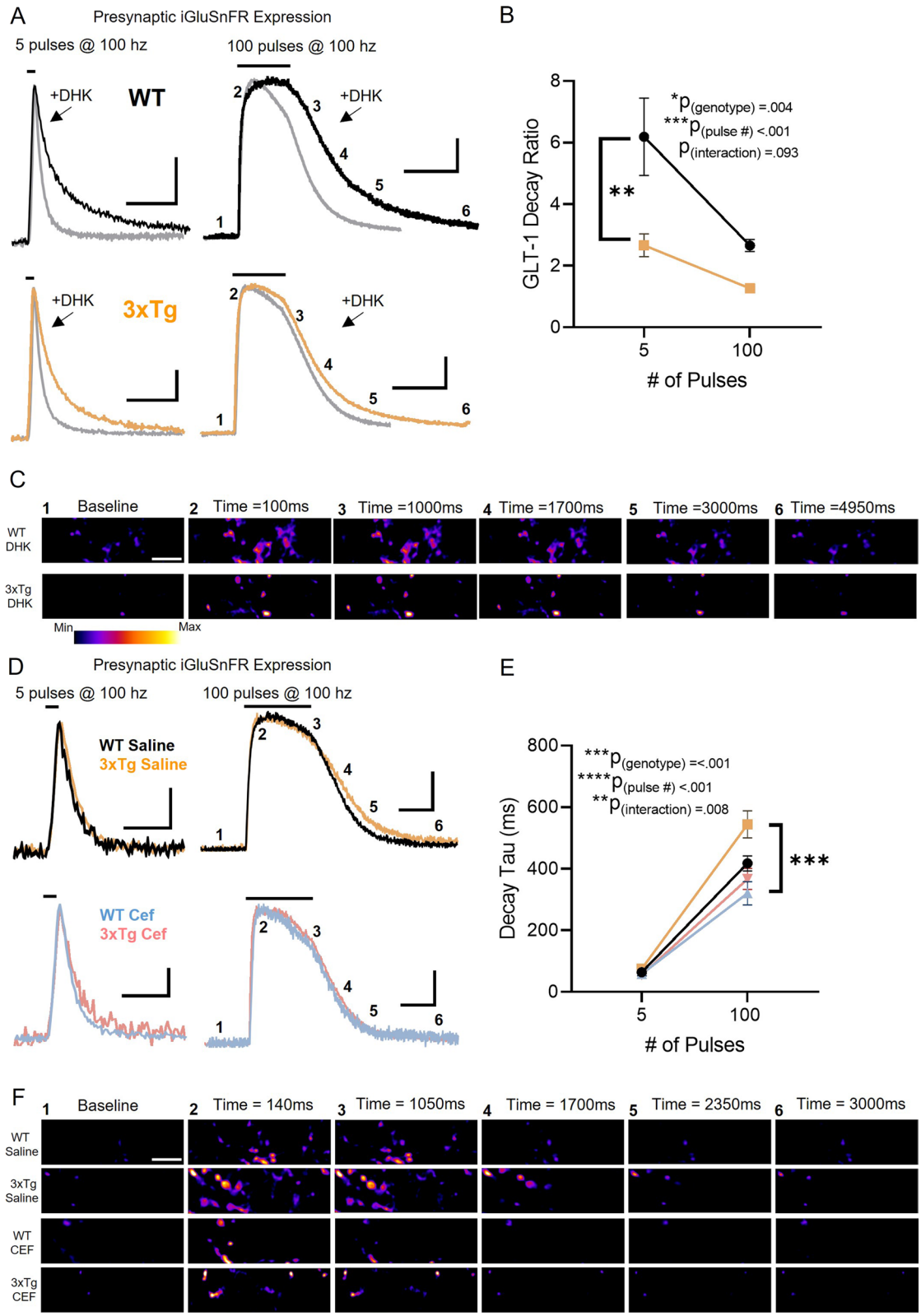

Fig. 4 (See legend on previous page.)

significance, it is worth pointing out that at 100 pulses, ceftriaxone tended to accelerate glutamate clearance in WT tissue while tending to slow clearance in 3xTg tissue, though the possible explanation for such tendencies are unclear at present. Together, these results suggest that GLT-1 can have both a reduced (presynaptic) and enhanced (postsynaptic) contribution to overall glutamate clearance in 3xTg mice, depending upon the microenvironment under study. Furthermore, our data suggest that GLT-1 upregulation may be beneficial in 3xTg mice by restoring presynaptic glutamate dynamics to WT levels.

Our DHK and ceftriaxone experiments suggested that GLT-1 impairments mediate the slow clearance rates observed at 3xTg presynaptic membranes. Nonetheless, we asked whether glutamate diffusion could differ between the genotypes and/or the pre- and postsynaptic microenvironments of interest in the present study. To this end, we applied a saturating concentration of the non-selective glutamate transporter blocker DL-TBOA (100 µM, applied in the presence of 50 µM D-APV and 20 µM DNQX). Under these conditions, iGluSnFR decay values are dramatically slowed compared to control levels, and primarily reflect the diffusion of glutamate away from the imaging ROI [27]. We found that relative glutamate diffusion rates, as estimated by iGluSnFR decay tau in the presence of saturating TBOA, were not significantly different between genotypes regardless of whether iGluSnFR expression was presynaptic (Additional file 1: Fig. 7A-C; WT $N=4$, $n=8$; 3xTg $N=6$, $n=8$; RM two-way ANOVA: $p_{\text{pulsenumber}}<0.001$; $p_{\text{genotype}}=0.650$; $p_{\text{interaction}}=0.058$) or postsynaptic (Additional file 1: Fig. 7D–F; WT $N=4$, $n=10$; 3xTg $N=5$, $n=9$; RM two-way ANOVA: $p_{\text{pulsenumber}}<0.001$; $p_{\text{genotype}}=0.263$; $p_{\text{interaction}}=0.810$). Similarly, iGluSnFR peak values in the presence of TBOA were not significantly different between genotypes for either presynaptic (Additional file 1: Fig. 8A; RM two-way ANOVA: $p_{\text{pulsenumber}}=0.010$; $p_{\text{genotype}}=0.808$; $p_{\text{interaction}}=0.865$) or postsynaptic expression (Additional file 1: Fig. 8B; RM two-way ANOVA: $p_{\text{pulsenumber}}<0.001$; $p_{\text{genotype}}=0.422$; $p_{\text{interaction}}=0.232$). Together with our previous results, the data suggest that poor GLT-1-mediated uptake, not poor diffusion, is primarily responsible for the slow glutamate clearance rates observed at 3xTg presynaptic membranes.

Slow glutamate clearance is also observed at glial membranes in 3xTg mice.

Our data suggest that GLT-1 dysfunction slows glutamate clearance primarily at presynaptic membranes in 3xTg mice. In contrast, glutamate clearance rates at postsynaptic membranes were similar between WT and 3xTg mice, consistent with the asymmetric glial coverage of tripartite synapses that enhances postsynaptic protection from spillover [14]. Next, we asked whether the observed uptake impairment exclusively impacted presynaptic membranes, or whether a more general approach to assess extrasynaptic glutamate levels could also detect slower clearance in 3xTg mice. Determining the precise microenvironments most susceptible to glutamate uptake impairments is of interest as glutamate receptors are located on glial cells in addition to their more canonical pre- and postsynaptic locations [42, 43]. We injected six-month-old WT and 3xTg mice with iGluSnFR as before, but this time iGluSnFR expression was restricted to astrocytes through the use of the GFAP promoter [44]. Similar to our results for presynaptic iGluSnFR expression, glutamate clearance rates were slower in 3xTg mice compared to WT (Additional file 1: Fig. 9; WT N = 3, n = 12; 3xTg N = 3, n = 10; RM two-way ANOVA: $p_{\text{pulsenumber}}<0.001$; $p_{\text{genotype}}=0.004$; $p_{\text{interaction}}=0.006$) with 3xTg mice being significantly slower at clearing glutamate at 100 pulses (Bonferroni: $p<0.001$). These results suggest that the slow glutamate clearance from the extracellular space in 3xTg mice primarily affects presynaptic and astrocytic membranes over postsynaptic dendrites.

(See figure on next page.)

Fig. 5 The GLT-1 contribution to glutamate clearance at postsynaptic microenvironments is elevated in 3xTg mice compared to WT. **A** Average postsynaptic iGluSnFR response to 5 (left) and 100 pulses (right) of electrical stimulation (100 Hz) in WT (top; black and grey) and 3xTg mice (bottom; orange and grey) before and after DHK application. Grey traces denote average iGluSnFR response before DHK application. **B** GLT-1 decay ratio in WT and 3xTg mice, calculated by the fold increase in iGluSnFR decay induced by a saturating concentration of the GLT-1 inhibitor DHK. **C** Representative images depicting the postsynaptic iGluSnFR response in the presence of DHK in WT (top row) and 3xTg (bottom row) mice evoked by 100 pulses of electrical stimulation (100 Hz). **D** Average postsynaptic iGluSnFR responses to 5 (left) and 100 pulses (right) of stimulation in WT-saline (black), 3xTg saline (orange), WT-ceftriaxone (Cef; blue), and 3xTg-ceftriaxone-treated mice (pink). **E** iGluSnFR decay tau in saline- or ceftriaxone-treated WT and 3xTg mice. **F** Representative images depicting the postsynaptic iGluSnFR response in WT-saline (top row), 3xTg-saline (second row), WT-ceftriaxone (third row), and 3xTg-ceftriaxone-treated mice (bottom row) evoked by 100 pulses of electrical stimulation (100 Hz). Black lines above iGluSnFR traces indicate the timing and duration of electrical stimulation. Scale bars in A: 10%ΔF/F, 500 ms (left) and 25%ΔF/F, 1000 ms (right). DHK traces scaled to match the peak of control (without DHK) traces. Scale bar in E: 10 µm. Scale bars in D: 10%ΔF/F, 200 ms (left) and 25%ΔF/F, 500 ms (right). 3xTg traces scaled to match the peak of WT traces. Error bars indicate s.e.m. *** $p<0.001$

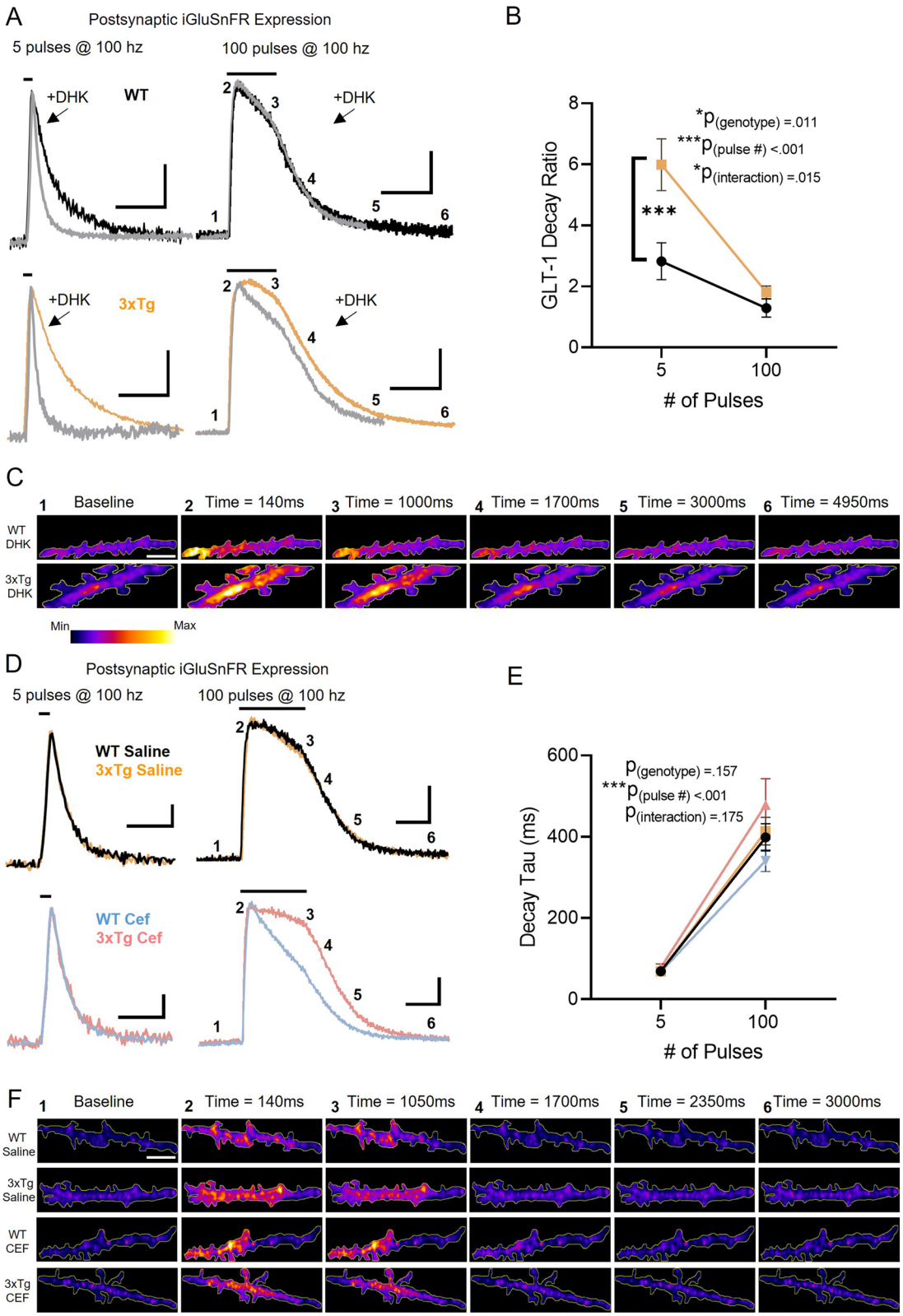

Fig. 5 (See legend on previous page.)

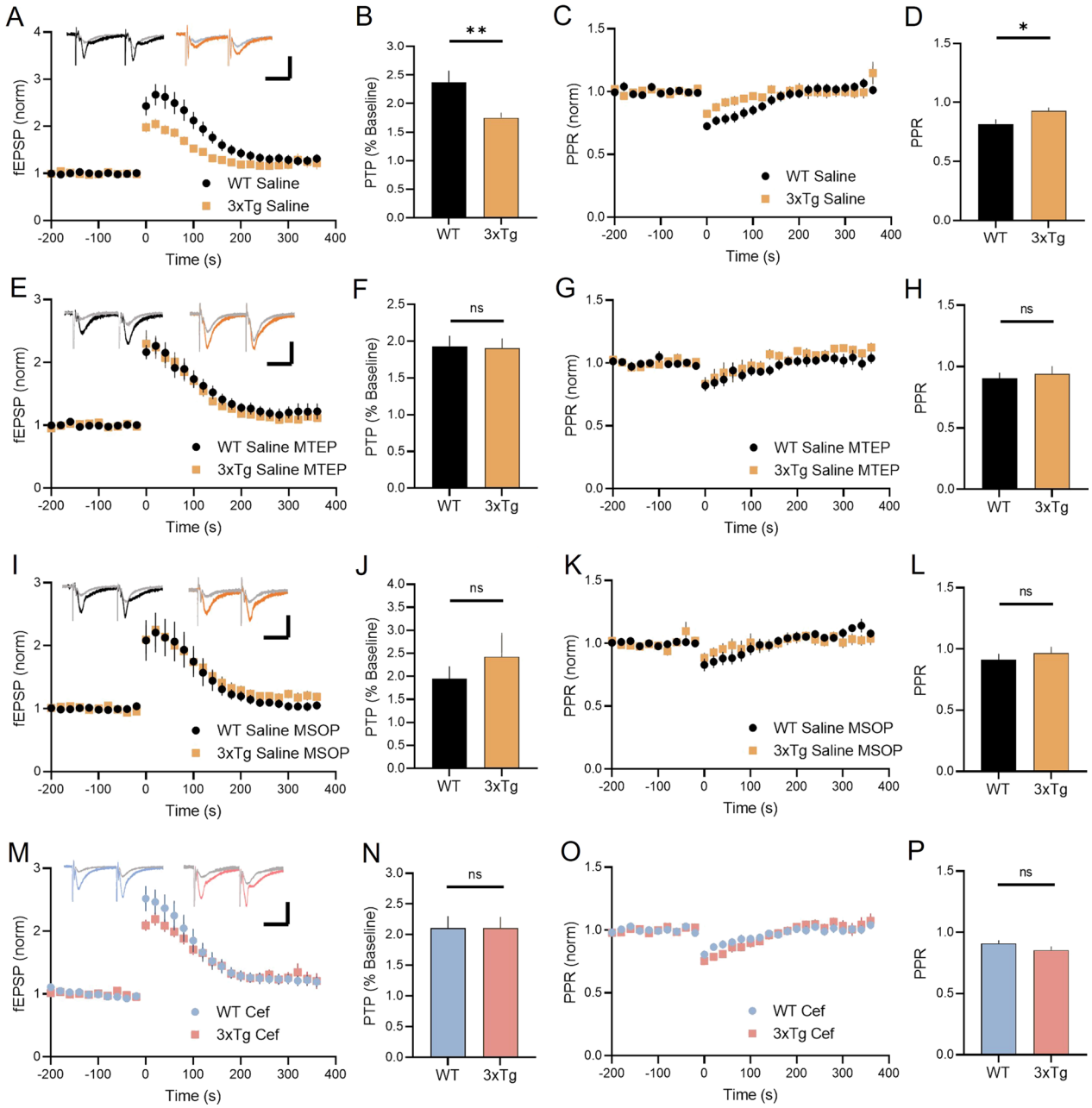

Fig. 6 mGluR antagonism or ceftriaxone is sufficient to prevent short-term plasticity impairment in 3xTg mice. **A** Post-tetanic potentiation (PTP) in acute slices from WT (black) and 3xTg (orange) mice. PTP is induced by high-frequency stimulation (HFS) at time = 0. **B** PTP is significantly decreased in 3xTg mice. **C** Paired-pulse ratio (PPR) in WT and 3xTg. **D** PPR changes after HFS are impaired in 3xTg mice. **E**–**H** PTP and PPR responses to HFS in WT and 3xTg mice during bath application of MTEP (100 μM). **I**–**L** PTP and PPR responses to HFS in WT and 3xTg mice during bath application of MSOP (100 μM). **M**–**P** PTP and PPR responses to HFS in WT and 3xTg mice treated with ceftriaxone. Scale bars: 25 ms, 500 μV. Error bars indicate s.e.m. *$p < 0.05$, ** $p < 0.01$. ns, not significant

Ceftriaxone or mGluR antagonists prevent short-term presynaptic plasticity deficits in the 3xTg hippocampus

The prolonged glutamate transients observed at presynaptic membranes in 3xTg mice suggest that GLT-1 dysfunction could promote presynaptic autoreceptor overactivation. To test this hypothesis, we examined post-tetanic potentiation (PTP), a form of short-term plasticity characterized by a temporary facilitation of presynaptic release [45]. PTP is impaired in 3xTg mice [46], though the underlying mechanisms of the impairment are poorly

understood. In acute hippocampal sections obtained from six-month-old WT and 3xTg mice, we found that PTP, induced by HFS (100 pulses, 1 s), was significantly impaired in 3xTg mice compared to WT (Fig. 6A, B; WT N = 6, $n = 15$; 3xTg N = 8, $n = 16$; t-test: $p = 0.009$). In WT slices, PTP was associated with an increase in release probability, as demonstrated by a reduced PPR immediately following HFS. The magnitude of the HFS-induced change in release probability was significantly reduced in 3xTg compared to WT mice (Fig. 6C, D; WT N = 6, $n = 15$; 3xTg N = 8, $n = 16$; t-test: $p = 0.031$). Next, we asked whether the release facilitation associated with PTP was opposed by glutamate autoreceptor overactivation in 3xTg mice. Presynaptic glutamate receptors known to exist at adult CA3-CA1 synapses include mGluR5 and mGluR7, both of which have been shown to negatively regulate glutamate release [47–50]. We found that PTP was no longer impaired in 3xTg mice compared to WT when we blocked mGluR5 (Fig. 6E-F; WT N = 5, n = 8; 3xTg N = 5, n = 10; t-test: $p = 0.888$) or mGluR7 (Fig. 6I, J; WT N = 5, $n = 10$; 3xTg N = 5, n = 11; t-test: $p = 0.434$) with MTEP or MSOP, respectively. In the presence of MTEP (Fig. 6G, H; t-test: $p = 0.667$) or MSOP (Fig. 6K, L; t-test: $p = 0.442$), HFS had a similar effect on release probability in WT and 3xTg mice. These data demonstrate that blockade of either mGluR5 or mGluR7 prevents the PTP impairment in 3xTg mice. As both mGluR5 and mGluR7 have been shown to be present presynaptically at CA3-CA1 synapses where they can negatively regulate glutamate release, we reasoned that the slow glutamate clearance may be required to promote their overactivation to oppose PTP. We have shown that ceftriaxone prevents the prolonged glutamate transients at 3xTg terminals; therefore, we also assessed PTP in ceftriaxone-treated mice in the absence of mGluR5 or mGluR7 blockade. Ceftriaxone alone was sufficient to prevent the PTP impairment in 3xTg mice (Fig. 6M, N; WT N = 5, $n = 13$; 3xTg $N = 5$, $n = 17$; t-test: $p = 0.995$). Analysis of PPR demonstrated that HFS had a similar effect on release probability in both WT and 3xTg mice after ceftriaxone treatment (Fig. 6O, P; t-test: $p = 0.225$). Overall, our data suggest that GLT-1 dysfunction prolongs glutamate actions at the presynapse in 3xTg mice, promoting autoreceptor-mediated opposition to presynaptic short-term plasticity. Blocking either mGluR5, mGluR7 or enhancing GLT-1 with ceftriaxone is sufficient to restore short-term plasticity to control levels.

Discussion

Here, we demonstrate that compromised GLT-1-mediated uptake, either through pharmacological inhibition or in the 3xTg mouse model of AD, slows glutamate clearance to a greater extent at presynaptic compared to postsynaptic membranes in the hippocampus. The asymmetric uptake deficit was demonstrated in multiple experimental 3xTg cohorts, including mice at different disease stages (6 and 12 months), different bath temperatures, and in saline- (but not ceftriaxone-) treated mice. Based on the asymmetrical glial coverage of tripartite synapses in the stratum radiatum, it was previously proposed that glutamate spillover should have a greater impact at the presynapse than the postsynapse [14, 15]. By visualizing glutamate dynamics independently in CA3 axons or CA1 dendrites, we provide strong functional data supporting such a presynaptic vulnerability to glutamate uptake impairments. Subsequent electrophysiological experiments suggest that the presynaptic vulnerability to GLT-1 impairment in 3xTg mice promotes autoreceptor-mediated opposition to short-term presynaptic plasticity.

Presynaptic vulnerability to GLT-1 dysfunction in 3xTg mice

GLT-1 reductions are widely reported in AD brains of human patients and animal models [10, 16–23]. We also observed reduced GLT-1 immunofluorescence in CA1 stratum radiatum of 3xTg mice in the present study. In this same model, previous work reported a GLT-1 decrease of about 50% at 6 months and 12 months, with levels declining even further by 23 months of age [51, 52]. The GLT-1 reduction at 6 and 12 months of age is consistent with our iGluSnFR imaging results demonstrating slower glutamate clearance at the presynaptic microenvironment at both ages. In contrast, GLAST expression remains stable in 3xTg mice up to at least 12 months of age [51], so GLAST impairments are unlikely to contribute to the clearance deficits observed in the present study.

GLT-1 is expressed as different isoforms, with the GLT-1a, GLT-1b, and GLT-1c isoforms making up roughly 90%, 6%, and 1% of the brain's total GLT-1 content, respectively [53–55]. GLT-1a is the isoform found in axon terminals [3, 54, 56] whereas both GLT-1a and GLT-1b are found in astrocytes [54, 57]. At present, it is uncertain whether the clearance deficit we observed in the current study is attributed to an impairment in axonal GLT-1, astrocytic GLT-1, or both. In support of axonal GLT-1 impairment, we found that ceftriaxone was able to rescue the clearance deficit at presynaptic membranes in 3xTg mice, and a previous study found that ceftriaxone increased axonal GLT-1 but not GLT-1 located on perisynaptic astrocytic processes [58]. Furthermore, axonal GLT-1 is the main contributor to uptake in synaptosome preparations [59], and synaptosomal glutamate uptake is impaired in AD tissue [60–62]. Neuronal GLT-1 knockout is sufficient to

produce late-onset cognitive deficits [63]. However, while axonal GLT-1 is known to contribute to presynaptic energy supply [64] and its presence can help protect from excitotoxic damage [65], its contribution to overall extracellular glutamate dynamics is poorly understood.

While ceftriaxone was found by Capuani and colleagues [58] to increase GLT-1 in axon terminals but not astrocytic perisynaptic processes, another study showed increased expression of both GLT-1a and GLT-1b following ceftriaxone treatment [66], and the latter is thought to localize to astrocytes and not nerve terminals [57]. As we found slower clearance rates in 3xTg mice at both presynaptic and glial membranes, it is conceivable that both axonal and astrocytic GLT-1 are impaired in this AD model. By combining the imaging approach used in the current study with cell type specific knockouts of GLT-1, future studies can better understand how presynaptic and astrocytic GLT-1 work together to shape the subcellular and temporal profile of extracellular glutamate transients. In addition, further work is required to determine whether the clearance deficit identified here in 3xTg mice is caused by an isoform- or cell type-specific impairment of GLT-1.

We found that ceftriaxone effectively restored glutamate dynamics at presynaptic membranes in 3xTg mice, but it was without significant effect on glutamate dynamics at the postsynaptic microenvironment, likely as no clearance deficit was ever observed at postsynaptic membranes. The lack of ceftriaxone effect postsynaptically is consistent with a study from our lab demonstrating that ceftriaxone has little effect on glutamate dynamics in healthy animals despite significantly increasing GLT-1 expression [30].

We used the DHK decay ratio as a measure of GLT-1's contribution to total uptake at a given microenvironment; the greater the effect of saturating DHK being indicative of a greater role for GLT-1 in promoting rapid glutamate clearance [27, 41]. It should be noted that GLT-1a and GLT-1b show a similar sensitivity to DHK [55], so we presumably inhibited both isoforms equally. In agreement with a presynaptic vulnerability to glutamate spillover in AD, saturating DHK had a reduced effect at presynaptic membranes of 3xTg mice compared to WT controls. Unexpectedly, the GLT-1 contribution to total glutamate uptake at the postsynaptic microenvironment was enhanced in 3xTg mice compared to WT controls. Thus, in 3xTg mice, GLT-1's role in glutamate uptake appears to be both impaired (presynaptic) and enhanced (postsynaptic) depending on the microenvironment in question. The precise mechanisms underlying this dichotomy remain to be addressed, but could represent a nanoscale malalignment of glial membranes, where the previously reported glial asymmetry favoring postsynaptic protection is exaggerated even further in 3xTg mice. It is important to note that the studies that have reported glial asymmetry—where glial coverage of the postsynapse exceeds that of the presynapse [14, 15]—used chemical fixation, which is now known to reduce the size of the extracellular space [67]. It is unknown whether this chemical fixation artifact affects the asymmetry numbers obtained in these studies. In either case, it is likely that the role of diffusion in clearing glutamate from synaptic sites has been underestimated, as further suggested by a recent paper that elegantly used iGluSnFR to quantify glutamate spread to neighboring synapses in the neuropil [68]. Importantly, at 6 months of age, the total volume of the extracellular space and its tortuosity are the same between WT and 3xTg mice [69], consistent with the conclusion that our observed effects are likely to be mediated by deficits in transporter-mediated uptake rather than altered diffusion. Using super-resolution imaging techniques, it is of interest for future studies to better understand the nanoscale spatial relationships between GLT-1 expression, perisynaptic astrocytic processes, and pre- and postsynaptic membranes in 3xTg mice.

Activity-dependent slowing of glutamate clearance

One notable feature of our iGluSnFR decay measures was that genotype differences were typically only detected after a longer train of neural activity was evoked with 100 pulses, and not with 5 pulses. A possible explanation for this finding is suggested by the concept of spare glutamate transporters [70], and that the glutamate released by 5 pulses is insufficient to overwhelm the glutamate uptake system. In other words, 3xTg mice still have sufficient GLT-1 protein to efficiently clear glutamate released by short bursts of activity. When glutamate transporters are challenged with HFS of longer duration (in this case, 1 s), uptake is slowed considerably. This activity-dependent slowing of glutamate clearance has been described previously [27, 35]. During longer trains of neural activity, potassium efflux and electrogenic transporter currents depolarize astrocytic processes, which reduces the driving force for glutamate uptake [71]. Blocking Kir4.1 on astrocytes prolongs the depolarization of perisynaptic astrocytic processes, seemingly by increasing the time required to restore extracellular potassium levels [71]. Interestingly, Kir4.1 expression is reduced in 3xTg mice and 3xTg astrocytes exhibit reduced swelling in response to a high potassium challenge [69], suggesting that activity-dependent slowing of glutamate clearance may be exaggerated in 3xTg mice due to poor Kir4.1-mediated potassium buffering.

While it is unlikely that a large population of Schaffer collaterals fire synchronously at 100 Hz for a full second

in the healthy brain [72], fast gamma oscillations in the 100 Hz range is observed in the hippocampus during REM sleep [73] and while encoding novel object-place pairings [74]. Additionally, neuronal hyperexcitability [12, 75, 76] and epilepsy have been associated with AD and evidence suggests that epileptic events can accelerate the progression of AD [77]. Starting from a very early age just after weaning, 3xTg mice are highly susceptible to audiogenic seizures, and bicuculline induces prolonged and more frequent ictal-like events in acute slices from 3xTg mice compared to WT [78]. Nonetheless, it is of great interest for future studies to test additional activity patterns, durations, and frequencies that more broadly cover the physiological range of activity, including theta burst stimulation, which is also known to cause activity-dependent slowing of glutamate clearance [28]. Such studies will help determine the precise conditions under which 3xTg presynaptic membranes are exposed to excess glutamate. Faster variants of the iGluSnFR sensor [79] may also be required to reveal more subtle deficits that may have gone undetected in the present study.

Differential regulation of glutamate dynamics at the subcellular level

In addition to their localization at pre- and postsynaptic membranes, glutamate receptors also exist on astrocytes. When we expressed iGluSnFR in astrocytes, we also observed slower uptake in 3xTg mice. Therefore, astrocytic glutamate receptors may also be vulnerable to overactivation in AD. Astrocytic NMDAR activation induces the release of pro-inflammatory cytokines, in particular TNF-alpha [80]. In addition to being a potent inflammatory cytokine, TNF-alpha is a powerful modulator of glutamate uptake, with TNF-alpha application to cultured astrocytes significantly reducing glutamate uptake [81], at least in part through a downregulation of glutamate transporters [82]. Importantly, TNF-alpha elevations are readily observed in the AD hippocampus [83–85]. Therefore, it is possible that GLT-1 deficits promote the overactivation of astrocytic NMDARs, driving the release of TNF-alpha. It is important to consider that there is still much we do not know about astrocytic glutamate receptors; as significant heterogeneity exists in both the morphology and function of astrocytes, it is possible that the distribution of glutamate receptors on astrocytes may differ across brain regions [86]. Indeed, astrocytic glutamate receptor activation has also been observed to confer neuroprotective roles in some studies [87, 88].

Slow uptake in the 3xTg hippocampus was found to primarily affect presynaptic over postsynaptic membranes, and our subsequent electrophysiology experiments suggest that CA3-CA1 autoreceptor overactivation may act to oppose presynaptically-mediated post-tetanic potentiation in 3xTg mice. mGluRs are powerful modulators of synaptic transmission and their dysfunction is implicated in epilepsy, schizophrenia, and AD [89]. While mGluR expression is present throughout the hippocampus, mGluR5 and mGluR7 are highly expressed in CA3 and their activation leads to a depression of CA3-CA1 synaptic neurotransmission [47–50]. Our electrophysiology experiments support this observation, as we found that PTP is decreased in 3xTg mice. Moreover, mGluR5 (MTEP) or mGluR7 (MSOP) antagonism restored PTP values to WT levels. Interestingly, ceftriaxone alone was sufficient to restore PTP to control levels, suggesting that the glutamate accumulation at 3xTg axons can overstimulate mGluR autoreceptors to oppose plasticity. It is well-known that synapse loss is one of the best correlates of cognitive decline in AD [90], and synapse loss in the hippocampus is reported in both preclinical and clinical studies of AD [91, 92]. Ceftriaxone administration was previously shown to restore synaptic protein expression and improve cognitive function in 3xTg mice, even when injected at an age of 10–12 months [51]. Similarly, transgenic and pharmacological approaches to increasing GLT-1 levels in the $APP_{sw,Ind}$ model of AD also improved cognitive function and synaptic protein expression [62]. Thus, an intriguing possibility is that a presynaptic vulnerability to glutamate spillover may promote subsequent synapse elimination and cognitive decline in AD.

A recent study demonstrated that plasticity-inducing stimuli causes the withdrawal of GLT-1-expressing astrocytic processes from synaptic sites [93]. Intriguingly, when the authors performed 3D super-resolution imaging of tripartite synapses using bassoon, Homer1, and GLT-1 antibodies, they found that GLT-1 withdrew from presynaptic (bassoon-positive) sites following the induction of chemical LTP. The activity-induced withdrawal of astrocytic processes increased the spread of extracellular optical glutamate transients in the stratum radiatum and promoted inter-synaptic crosstalk that enhanced NMDAR activity at inactive synapses. In the stratum radiatum, the inter-synapse distance is approximately 0.5 µm [94], and it was recently demonstrated that that hippocampal neuropil may be more permissive than previously thought; synaptically-released glutamate can activate iGluSnFR expressed on inactive synapses at distances > 1.5 µm from the active synapse [68]. Thus, while the present data demonstrate slower glutamate clearance at presynaptic terminals, our findings cannot completely rule out abnormalities that may be occurring at the postsynaptic membrane. Any slowing of glutamate clearance at the postsynaptic membrane may be too subtle to be detected by the

iGluSnFR biosensor used, and our postsynaptic imaging and analysis approach was not designed to assess the spatial spread of an active synapse to the postsynaptic membrane of an inactive, neighboring synapse. If GLT-1-expressing astrocytic processes have withdrawn from presynaptic sites in the 3xTg mice used in the present study, it is plausible to suggest that in addition to presynaptic autoreceptor overactivation, there may also be excessive spillover to both pre- and postsynaptically-located glutamate receptors at neighboring synapses. Thus, it is of interest for future studies to explore the extent of inter-synaptic crosstalk in the context of AD. As a high transporter density helps to restrict the spatial spread of glutamate in the neuropil [68], it is likely that the GLT-1 reduction in 3xTg mice promotes excessive inter-synaptic crosstalk.

Summary and conclusions

By isolating the study of extracellular glutamate dynamics at pre- or postsynaptic microenvironments, we have revealed a functional consequence of the asymmetric morphological arrangement of astrocytes first described almost two decades ago by Lehre and Rusakov [14]. Despite an often postsynaptic-centric view of the consequences of glutamate spillover in disease [65], we reveal a presynaptic vulnerability to GLT-1 impairment in the 3xTg model of AD that opposes short-term potentiation at CA3-CA1 synapses. Our results shed new light on the consequences of GLT-1 dysfunction in AD and may have broader implications for presynaptic vulnerability in a range of disease states associated with GLT-1 reduction.

Supplementary Information

The online version contains supplementary material available at https://doi.org/10.1186/s40478-023-01524-x.

Additional file 1. **Figure 1**. NMDA receptor blockade reduces postsynaptic but not presynaptic calcium responses to high-frequency stimulation. (A) Presynaptic GCaMP6f response to high-frequency stimulation (HFS) before (black) and after (blue) bath application of d-APV (50 µM). **B** Postsynaptic GCaMP6f response to HFS before (black) and after (orange) d-APV. **C** postsynaptic GCaMP responses are more sensitive to NMDAR blockade than presynaptic GCaMP responses, with a 50% reduction observed in the postsynaptic GCaMP response. Error bars represent s.e.m. *** $p < 0.001$. **Figure 2**: GLT-1 expression is significantly reduced in 3xTg hippocampus. WT and 3xTg mice were perfused at 6 months of age. GLT-1 intensity was quantified in stratum radiatum. All immunostaining was performed at the same time and imaging parameters (LED intensity, exposure times) remained consistent for both genotypes. WT $n = 12$, 3xTg $n = 10$. Scale bar in A: 50 µm. Error bars represent s.e.m. ** $p < 0.01$. **Figure 3**. Peak iGluSnFR responses do not differ between WT and 3xTg mice. **A** Postsynaptic iGluSnFR response peaks in WT (black) and 3xTg (orange) mice. **B** Presynaptic iGluSnFR response peaks in WT (black) and 3xTg (orange) mice. **Figure 4**. iGluSnFR dynamics at individual iGluSnFR-positive puncta are slower to decay in 3xTg mice. (A) Representative image showing presynaptic iGluSnFR expression. ROIs are drawn around individual iGluSnFR puncta representing putative single synapses. **B** Representative iGluSnFR responses to electrical stimulation (100 pulses, 100 Hz, indicated by the black line above the traces). **C** Box-and-whisker plots of putative single synapse decay tau values following stimulation. Individual ROI responses are shown as dots within the plot. (D) Cumulative distribution plot of the decay tau values at the quantified ROIs. Scale bar in A: 10 µm. *** $p < 0.001$, **** $p < 0.0001$. **Figure 5**. Presynaptic glutamate clearance impairment and spared postsynaptic clearance in the 3xTg hippocampus replicated at 32 degrees. **A**–**C** Postsynaptic iGluSnFR expression (A). Average traces in WT (black) and 3xTg mice (orange) in response to 5 (B, left) or 100 (B, right) pulses of evoked activity. Grouped data are shown in C. **D**–**F** Same as A-C but for presynaptic iGluSnFR expression. All experiments conducted in ACSF heated to 32 ℃. Horizontal lines above iGluSnFR traces indicate the timing and duration of electrical stimulation. Scale bars in B and E: 10 %ΔF/F, 200 ms (left) and 20 %ΔF/F, 500 ms (right). 3xTg traces scaled to match the peak of WT traces. Traces in boxes show average iGluSnFR responses normalized to the value at the end of the one second of electrical stimulation. Error bars represent s.e.m. *$p < 0.05$, ***$p < 0.001$. **Figure 6**. Peak iGluSnFR responses do not differ between WT and 3xTg mice after GLT-1 blockade with DHK. **A** Presynaptic iGluSnFR response peaks in WT (black) and 3xTg (orange) mice. **B** Postsynaptic iGluSnFR response peaks in WT (black) and 3xTg (orange) mice. Response peaks were obtained in the presence of a saturating concentration (300 µM) of the GLT-1 inhibitor DHK. **Figure 7**. Diffusion does not differ between WT and 3xTg mice. (A-C) Presynaptic iGluSnFR responses to 5 (A) and 100 (B) pulses in the presence of 100 µM TBOA to block transporter-mediated uptake. **D**-**F** Same for A-C but for postsynaptic iGluSnFR expression. Horizontal lines above iGluSnFR traces indicate the timing and duration of electrical stimulation. Scale bars in A and D: 10 %ΔF/F, 1000 ms. Scale bars in B and E: 25 %ΔF/F, 2000 ms. 3xTg traces scaled to match the peak of WT traces. Traces in boxes show average iGluSnFR responses normalized to the value at the end of the one second of electrical stimulation. Error bars represent s.e.m. **Figure 8**. Peak iGluSnFR responses do not differ between WT and 3xTg mice after non-selective glutamate transporter blockade with TBOA. **A** Presynaptic iGluSnFR response peaks in WT (black) and 3xTg (orange) mice. **B** Postsynaptic iGluSnFR response peaks in WT (black) and 3xTg (orange) mice. Response peaks were obtained in the presence of a saturating concentration (100 µM) of the glutamate transporter inhibitor TBOA. **Figure 9**. Glutamate clearance is significantly slower in astrocytes of the 3xTg hippocampus. **A** Schematic of GFAP-iGluSnFR. **B** Average iGluSnFR responses to 5 (left) and 100 (right) pulses of stimulation in WT (black) and 3xTg (orange) mice. Grouped data shown in (**C**). Horizontal lines above iGluSnFR traces indicate the timing and duration of electrical stimulation. Scale bar in B: 10 %ΔF/F, 200 ms. Scale bar in C: 25 %ΔF/F, 500 ms. 3xTg traces scaled to match the peak of WT traces. Traces in box show average iGluSnFR responses normalized to the value at the end of the one second of electrical stimulation. Error bars represent s.e.m. *** $p < 0.001$.

Acknowledgements

The authors would like to thank the animal care staff at Memorial's animal care facility for their assistance with animal housing and colony maintenance.

Funding

This research was funded by grants from the Alzheimer's Society of Canada (New Investigator Award), Suncor (Terra Nova Young Innovator Award) and the Natural Sciences and Engineering Research Council of Canada (Discovery Grant).

Declarations

Competing interests

The authors have no competing interests.

Received: 9 December 2022 Accepted: 28 January 2023
Published online: 14 February 2023

References

1. Danbolt NC (2001) Glutamate uptake. Prog Neurobiol 65:1–105
2. Lehre KP, Danbolt NC (1998) The number of glutamate transporter subtype molecules at glutamatergic synapses: chemical and stereological quantification in young adult rat brain. J Neurosci 18:8751–8757
3. Rimmele TS, Rosenberg PA (2016) GLT-1: the elusive presynaptic glutamate transporter. Neurochem Int 98:19–28
4. Benarroch EE (2018) Glutamatergic synaptic plasticity and dysfunction in Alzheimer disease: emerging mechanisms. Neurology 91:125–32
5. Bukke VN, Archana M, Villani R, Romano AD, Wawrzyniak A, Balawender K et al (2020) The dual role of glutamatergic neurotransmission in Alzheimer's disease: from pathophysiology to pharmacotherapy. Int J Mol Sci 21:1–29
6. Esposito Z, Belli L, Toniolo S, Sancesario G, Bianconi C, Martorana A (2013) Amyloid beta, glutamate, excitotoxicity in Alzheimer's disease: Are we on the right track? CNS Neurosci Ther 19:549–555
7. Li S, Selkoe DJ (2020) A mechanistic hypothesis for the impairment of synaptic plasticity by soluble Aβ oligomers from Alzheimer's brain. J Neurochem 154:583–597
8. Parsons MP, Raymond LA (2014) Extrasynaptic NMDA receptor involvement in central nervous system disorders. Neuron 82:279–293
9. Rudy CC, Hunsberger HC, Weitzner DS, Reed MN (2015) The role of the tripartite glutamatergic synapse in the pathophysiology of Alzheimer's disease. Aging Dis 6:131–148
10. Wang R, Reddy PH (2017) Role of glutamate and NMDA receptors in Alzheimer's disease. J Alzheimer's Dis 57:1041–1048
11. Lewerenz J, Maher P (2015) Chronic glutamate toxicity in neurodegenerative diseases-What is the evidence? Front Neurosci 9:1–20
12. Zott B, Konnerth A (2023) Impairments of glutamatergic synaptic transmission in Alzheimer's disease. Semin Cell Dev Biol 139:24–34
13. Danbolt NC, Furness DN, Zhou Y (2016) Neuronal vs glial glutamate uptake: resolving the conundrum. Neurochem Int 98:29–45
14. Lehre KR, Rusakov DA (2002) Asymmetry of glia near central synapses favors presynaptically directed glutamate escape. Biophys J 83:125–134
15. Gavrilov N, Golyagina I, Brazhe A, Scimemi A, Turlapov V, Semyanov A (2018) Astrocytic coverage of dendritic spines, dendritic shafts, and axonal boutons in hippocampal neuropil. Front Cell Neurosci 12:1–16
16. Ferrarese C, Begni B, Canevari C, Zoia C, Piolti R, Frigo M et al (2000) Glutamate uptake is decreased in platelets from Alzheimer's disease patients. Ann Neurol 47:641–643
17. Hefendehl JK, LeDue J, Ko RWY, Mahler J, Murphy TH, MacVicar BA (2016) Mapping synaptic glutamate transporter dysfunction in vivo to regions surrounding Aβ plaques by iGluSnFR two-photon imaging. Nat Commun 7:13441
18. Li S, Hong S, Shepardson NE, Walsh DM, Shankar GM, Selkoe D (2009) Soluble oligomers of amyloid β protein facilitate hippocampal long-term depression by disrupting neuronal glutamate uptake. Neuron 62:788–801
19. Masliah E, Alford M, DeTeresa R, Mallory M, Hansen L (1996) Deficient glutamate transport is associated with neurodegeneration in Alzheimer's disease. Ann Neurol 40:759–766
20. Mookherjee P, Green PS, Watson GS, Marques MA, Tanaka K, Meeker KD et al (2011) GLT-1 loss accelerates cognitive deficit onset in an Alzheimer's disease animal model. J Alzheimer's Dis 26:447–455
21. Schallier A, Smolders I, Van Dam D, Loyens E, De Deyn PP, Michotte A et al (2011) Region- and age-specific changes in glutamate transport in the AβPP23 mouse model for Alzheimer's disease. J Alzheimer's Dis JAD 24:287–300
22. Scimemi A, Meabon JS, Woltjer RL, Sullivan JM, Diamond JS, Cook DG (2013) Amyloid-β1-42 slows clearance of synaptically released glutamate by mislocalizing astrocytic GLT-1. J Neurosci 33:5312–5318
23. Scott HA, Gebhardt FM, Mitrovic AD, Vandenberg RJ, Dodd PR (2011) Glutamate transporter variants reduce glutamate uptake in Alzheimer's disease. Neurobiol Aging 32:553.e1-553.e11
24. Brymer KJ, Barnes JR, Parsons MP (2021) Entering a new era of quantifying glutamate clearance in health and disease. J Neurosci Res. https://doi.org/10.1002/jnr.24810
25. Takahashi K, Foster JB, Lin CLG (2015) Glutamate transporter EAAT2: regulation, function, and potential as a therapeutic target for neurological and psychiatric disease. Cell Mol Life Sci 72:3489–3506
26. Oddo S, Caccamo A, Shepherd JD, Murphy MP, Golde TE, Kayed R et al (2003) Triple-transgenic model of Alzheimer's disease with plaques and tangles: intracellular Aβ and synaptic dysfunction. Neuron 39:409–421
27. Pinky NF, Wilkie CM, Barnes JR, Parsons MP (2018) Region-and activity-dependent regulation of extracellular glutamate. J Neurosci 38:5351–5366
28. Barnes JR, Mukherjee B, Rogers BC, Nafar F, Gosse M, Parsons MP (2020) The relationship between glutamate dynamics and activity-dependent synaptic plasticity. J Neurosci 40:2793–2807
29. Botterill JJ, Gerencer KJ, Vinod KY, Alcantara-Gonzalez D, Scharfman HE (2021) Dorsal and ventral mossy cells differ in their axonal projections throughout the dentate gyrus of the mouse hippocampus. Hippocampus 31:522–539
30. Wilkie CM, Barron JC, Brymer KJ, Barnes JR, Nafar F, Parsons MP (2021) The effect of GLT-1 upregulation on extracellular glutamate dynamics. Front Cell Neurosci 15:1–16
31. Wilkie CM, Barnes JR, Benson CLM, Brymer KJ, Nafar F, Parsons MP (2020) Hippocampal synaptic dysfunction in a mouse model of huntington disease is not alleviated by ceftriaxone treatment. Eneuro. https://doi.org/10.1523/ENEURO.0440-19.2020
32. Ting JT, Lee BR, Chong P, Soler-Llavina G, Cobbs C, Koch C et al (2018) Preparation of acute brain slices using an optimized N-Methyl-D-glucamine protective recovery method. JoVE J Vis Exp 132:e53825
33. Gao JX, Liu LZ, Liu C, Fan SJ, Liu LR, Liu SF et al (2020) GLT-1 knockdown inhibits ceftriaxone-mediated improvements on cognitive deficits, and GLT-1 and xCT expression and activity in APP/PS1 AD mice. Front Aging Neurosci 12:1–12
34. Lazic SE (2010) The problem of pseudoreplication in neuroscientific studies: Is it affecting your analysis? BMC Neurosci 11:5
35. Armbruster M, Hanson E, Dulla CG (2016) Glutamate clearance is locally modulated by presynaptic neuronal activity in the cerebral cortex. J Neurosci 36:10404–10415
36. Unger F, Konnerth A, Zott B (2021) Population imaging of synaptically released glutamate in mouse hippocampal slices. STAR Protoc 2:100877
37. Malenka RC, Bear MF (2004) LTP and LTD: an embarrassment of riches. Neuron 44:5–21
38. Nicoll RA, Review A (2017) Brief history of long-term potentiation. Neuron 93:281–90
39. Diamond JS, Jahr CE (2000) Synaptically released glutamate does not overwhelm transporters on hippocampal astrocytes during high-frequency stimulation. J Neurophysiol 83:2835–2843
40. Stover KR, Campbell MA, Van Winssen CM, Brown RE (2015) Early detection of cognitive deficits in the 3xTg-AD mouse model of Alzheimer's disease. Behav Brain Res 289:29–38
41. Hanson E, Armbruster M, Cantu D, Andresen L, Taylor A, Danbolt NC et al (2015) Astrocytic glutamate uptake is slow and does not limit neuronal NMDA receptor activation in the neonatal neocortex. Glia 63:1784–1796
42. Lalo U, Koh W, Lee CJ, Pankratov Y (2021) The tripartite glutamatergic synapse. Neuropharmacology 199:108758
43. Skowrońska K, Obara-Michlewska M, Zielińska M, Albrecht J (2019) NMDA receptors in astrocytes: in search for roles in neurotransmission and astrocytic homeostasis. Int J Mol Sci 20:309
44. Marvin JS, Borghuis BG, Tian L, Cichon J, Harnett MT, Akerboom J et al (2013) An optimized fluorescent probe for visualizing glutamate neurotransmission. Nat Methods 10:162–170
45. Zucker RS, Regehr WG (2002) Short-term synaptic plasticity. Annu Rev Physiol 64:355–405
46. Chakroborty S, Hill ES, Christian DT, Helfrich R, Riley S, Schneider C et al (2019) Reduced presynaptic vesicle stores mediate cellular and network plasticity defects in an early-stage mouse model of Alzheimer's disease. Mol Neurodegener 7:1–22
47. Gereau RW IV, Conn PJ (1995) Multiple presynaptic metabotropic glutamate receptors modulate excitatory and inhibitory synaptic transmission in hippocampal area CA1. J Neurosci 15:6879–6889
48. He Y, Wei M, Wu Y, Qin H, Li W, Ma X et al (2019) Amyloid β oligomers suppress excitatory transmitter release via presynaptic depletion of phosphatidylinositol-4,5-bisphosphate. Nat Commun. https://doi.org/10.1038/s41467-019-09114-z
49. Pittaluga A (2016) Presynaptic release-regulating mGlu1 receptors in central nervous system. Front Pharmacol 7:1–15

50. Shigemoto R, Kinoshita A, Wada E, Nomura S, Ohishi H, Takada M et al (1997) Differential presynaptic localization of metabotropic glutamate receptor subtypes in the rat hippocampus. J Neurosci 17:7503–7522
51. Zumkehr J, Rodriguez-Ortiz CJ, Cheng D, Kieu Z, Wai T, Hawkins C et al (2015) Ceftriaxone ameliorates tau pathology and cognitive decline via restoration of glial glutamate transporter in a mouse model of Alzheimer's disease. Neurobiol Aging 36:2260–71
52. Cao H, Zuo C, Gu Z, Huang Y, Yang Y, Zhu L et al (2022) High frequency repetitive transcranial magnetic stimulation alleviates cognitive deficits in 3xTg-AD mice by modulating the PI3K/Akt/GLT-1 axis. Redox Biol 54:102354
53. Ryan RM, Ingram SL, Scimemi A (2021) Regulation of glutamate, GABA and dopamine transporter uptake, surface mobility and expression. Front Cell Neurosci 15:670346
54. Berger UV, DeSilva TM, Chen W, Rosenberg PA (2005) Cellular and subcellular mRNA localization of glutamate transporter isoforms GLT1a and GLT1b in rat brain by in situ hybridization. J Comp Neurol 492:78–89
55. Chen W, Aoki C, Mahadomrongkul V, Gruber CE, Wang GJ, Blitzblau R et al (2002) Expression of a variant form of the glutamate transporter GLT1 in neuronal cultures and in neurons and astrocytes in the rat brain. J Neurosci 22:2142–2152
56. Chen W, Mahadomrongkul V, Berger UV, Bassan M, DeSilva T, Tanaka K et al (2004) The glutamate transporter GLT1a is expressed in excitatory axon terminals of mature hippocampal neurons. J Neurosci 24:1136–1148
57. Holmseth S, Scott HA, Real K, Lehre KP, Leergaard TB, Bjaalie JG et al (2009) The concentrations and distributions of three C-terminal variants of the GLT1 (EAAT2; slc1a2) glutamate transporter protein in rat brain tissue suggest differential regulation. Neuroscience 162:1055–1071
58. Capuani C, Melone M, Tottene A, Bragina L, Crivellaro G, Santello M et al (2016) Defective glutamate and K + clearance by cortical astrocytes in familial hemiplegic migraine type 2. EMBO Mol Med 8:967–986
59. Petr GT, Sun Y, Frederick NM, Zhou Y, Dhamne SC, Hameed MQ et al (2015) Conditional deletion of the glutamate transporter GLT-1 reveals that astrocytic GLT-1 protects against fatal epilepsy while neuronal GLT-1 contributes significantly to glutamate uptake into synaptosomes. J Neurosci 35:5187–5201
60. Hardy J, Cowburn R, Barton A, Reynolds G, Lofdahl E, O'Carroll A-M et al (1987) Region-specific loss of glutamate innervation in Alzheimer's disease. Neurosci Lett 73:77–80
61. Lauderback CM, Hackett JM, Huang FF, Keller JN, Szweda LI, Markesbery WR et al (2001) The glial glutamate transporter, GLT-1, is oxidatively modified by 4-hydroxy-2-nonenal in the Alzheimer's disease brain: the role of Aβ1–42. J Neurochem 78:413–416
62. Takahashi K, Kong Q, Lin Y, Stouffer N, Schulte DA, Lai L et al (2015) Restored glial glutamate transporter EAAT2 function as a potential therapeutic approach for Alzheimer's disease. J Exp Med 212:319–332
63. Sharma A, Kazim SF, Larson CS, Ramakrishnan A, Gray JD, McEwen BS et al (2019) Divergent roles of astrocytic versus neuronal EAAT2 deficiency on cognition and overlap with aging and Alzheimer's molecular signatures. Proc Natl Acad Sci U.S.A. 116:21800–21811
64. McNair LF, Andersen JV, Aldana BI, Hohnholt MC, Nissen JD, Sun Y et al (2019) Deletion of neuronal GLT-1 in mice reveals its role in synaptic glutamate homeostasis and mitochondrial function. J Neurosci 39:4847–4863
65. Rimmele TS, Li S, Andersen JV, Westi EW, Rotenberg A, Wang J et al (2021) Neuronal loss of the glutamate transporter glt-1 promotes excitotoxic injury in the hippocampus. Front Cell Neurosci. https://doi.org/10.3389/fncel.2021.788262
66. Alhaddad H, Das SC, Sari Y (2014) Effects of ceftriaxone on ethanol intake: a possible role for xCT and GLT-1 isoforms modulation of glutamate levels in P rats. Psychopharmacology 231:4049–4057
67. Korogod N, Petersen CC, Knott GW (2015) Ultrastructural analysis of adult mouse neocortex comparing aldehyde perfusion with cryo fixation. In: Häusser M (ed) eLife. eLife Sciences Publications Ltd, Cambridge, p e05793
68. Matthews EA, Sun W, McMahon SM, Doengi M, Halka L, Anders S et al (2022) Optical analysis of glutamate spread in the neuropil. Cereb Cortex 32:3669–3689
69. Tureckova J, Kamenicka M, Kolenicova D, Filipi T, Hermanova Z, Kriska J et al (2021) Compromised astrocyte swelling/volume regulation in the hippocampus of the triple transgenic mouse model of Alzheimer's disease. Front Aging Neurosci 13:783120
70. de Belo Nascimento I, Damblon J, Ingelbrecht C, Goursaud S, Massart M, Dumont A et al (2021) Pharmacological evidence for the concept of spare glutamate transporters. Neurochem Int 149:105142
71. Armbruster M, Naskar S, Garcia JP, Sommer M, Kim E, Adam Y et al (2022) Neuronal activity drives pathway-specific depolarization of peripheral astrocyte processes. Nat Neurosci 25:607–616
72. Albensi BC, Oliver DR, Toupin J, Odero G (2007) Electrical stimulation protocols for hippocampal synaptic plasticity and neuronal hyper-excitability: Are they effective or relevant? Exp Neurol 204:1–13
73. Bergel A, Deffieux T, Demené C, Tanter M, Cohen I (2018) Local hippocampal fast gamma rhythms precede brain-wide hyperemic patterns during spontaneous rodent REM sleep. Nat Commun 9:5364
74. Zheng C, Bieri KW, Hwaun E, Colgin LL (2016) Fast gamma rhythms in the hippocampus promote encoding of novel object–place pairings. ENeuro. https://doi.org/10.1523/ENEURO.0001-16.2016
75. Busche MA, Chen X, Henning HA, Reichwald J, Staufenbiel M, Sakmann B et al (2012) Critical role of soluble amyloid-β for early hippocampal hyperactivity in a mouse model of Alzheimer's disease. Proc Nat Acad Sci 109:8740–5
76. Zott B, Simon MM, Hong W, Unger F, Chen-Engerer HJ, Frosch MP et al (2019) A vicious cycle of β amyloid—dependent neuronal hyperactivation. Science (New York, NY) 365:559–565
77. Vossel KA, Tartaglia MC, Nygaard HB, Zeman AZ, Miller BL (2017) Epileptic activity in Alzheimer's disease: causes and clinical relevance. Lancet Neurol 16:311–322
78. Kazim SF, Chuang S-C, Zhao W, Wong RKS, Bianchi R, Iqbal K (2017) Early-onset network hyperexcitability in presymptomatic Alzheimer's disease transgenic mice is suppressed by passive immunization with anti-human APP/Aβ antibody and by mGluR5 Blockade. Front Aging Neurosci 9:71
79. Marvin JS, Scholl B, Wilson DE, Podgorski K, Kazemipour A, Müller JA et al (2018) Stability, affinity, and chromatic variants of the glutamate sensor iGluSnFR. Nat Methods 15:936–939
80. Sühs K-W, Gudi V, Eckermann N, Fairless R, Pul R, Skripuletz T et al (2016) Cytokine regulation by modulation of the NMDA receptor on astrocytes. Neurosci Lett 629:227–233
81. Ye ZC, Sontheimer H (1996) Cytokine modulation of glial glutamate uptake: a possible involvement of nitric oxide. NeuroReport 7:2181–2185
82. Zou JY, Crews FT (2005) TNF alpha potentiates glutamate neurotoxicity by inhibiting glutamate uptake in organotypic brain slice cultures: neuroprotection by NF kappa B inhibition. Brain Res 1034:11–24
83. Jayaraman A, Htike TT, James R, Picon C, Reynolds R (2021) TNF-mediated neuroinflammation is linked to neuronal necroptosis in Alzheimer's disease hippocampus. Acta Neuropathol Commun 9:159
84. Naghibi S, Shariatzadeh Joneydi M, Barzegari A, Davoodabadi A, Ebrahimi A, Eghdami E et al (2021) Treadmill exercise sex-dependently alters susceptibility to depression-like behaviour, cytokines and BDNF in the hippocampus and prefrontal cortex of rats with sporadic Alzheimer-like disease. Physiol Behav 241:113595
85. Zhao M, Cribbs DH, Anderson AJ, Cummings BJ, Su JH, Wasserman AJ et al (2003) The induction of the TNFalpha death domain signaling pathway in Alzheimer's disease brain. Neurochem Res 28:307–318
86. Höft S, Griemsmann S, Seifert G, Steinhäuser C (2014) Heterogeneity in expression of functional ionotropic glutamate and GABA receptors in astrocytes across brain regions: insights from the thalamus. Philos Trans R Soc Lond B Biol Sci 369:20130602
87. Durand D, Carniglia L, Beauquis J, Caruso C, Saravia F, Lasaga M (2014) Astroglial mGlu3 receptors promote alpha-secretase-mediated amyloid precursor protein cleavage. Neuropharmacology 79:180–189
88. Jimenez-Blasco D, Santofimia-Castaño P, Gonzalez A, Almeida A, Bolaños JP (2015) Astrocyte NMDA receptors' activity sustains neuronal survival through a Cdk5-Nrf2 pathway. Cell Death Differ 22:1877–1889
89. Cosgrove KE, Galván EJ, Barrionuevo G, Meriney SD (2011) mGluRs modulate strength and timing of excitatory transmission in hippocampal area CA3. Mol Neurobiol 44:93–101
90. Colom-Cadena M, Spires-Jones T, Zetterberg H, Blennow K, Caggiano A, Dekosky ST et al (2020) The clinical promise of biomarkers of synapse damage or loss in Alzheimer's disease. Alzheimer's Res Ther 12:1–12

91. Leshchyns'ka I, Liew HT, Shepherd C, Halliday GM, Stevens CH, Ke YD et al (2015) Aβ-dependent reduction of NCAM2-mediated synaptic adhesion contributes to synapse loss in Alzheimer's disease. Nat commun 6:8836
92. Neuman KM, Molina-Campos E, Musial TF, Price AL, Oh K-J, Wolke ML et al (2015) Evidence for Alzheimer's disease-linked synapse loss and compensation in mouse and human hippocampal CA1 pyramidal neurons. Brain Struct Funct 220:3143–3165
93. Henneberger C, Bard L, Panatier A, Reynolds JP, Kopach O, Medvedev NI et al (2020) LTP induction boosts glutamate spillover by driving withdrawal of perisynaptic astroglia. Neuron. https://doi.org/10.1016/j.neuron.2020.08.030
94. Rusakov DA, Kullmann DM (1998) Extrasynaptic glutamate diffusion in the hippocampus: ultrastructural constraints, uptake, and receptor activation. J Neurosci 18:3158–3170

Publisher's Note

Springer Nature remains neutral with regard to jurisdictional claims in published maps and institutional affiliations.

Ready to submit your research? Choose BMC and benefit from:

- fast, convenient online submission
- thorough peer review by experienced researchers in your field
- rapid publication on acceptance
- support for research data, including large and complex data types
- gold Open Access which fosters wider collaboration and increased citations
- maximum visibility for your research: over 100M website views per year

At BMC, research is always in progress.

Learn more biomedcentral.com/submissions

BMC